

1 **Exploration of the atmospheric chemistry of nitrous acid in a coastal** 2 **city of southeastern China: Results from measurements across four** 3 **seasons**

4

5 **Baoye Hu^{1,2,3,4} #, Jun Duan⁵ #, Youwei Hong^{1,2}, Lingling Xu^{1,2}, Mengren Li^{1,2}, Yahui Bian^{1,2}, Min**
6 **Qin^{5*}, Wu Fang⁵, Pinhua Xie^{1,5,6,7}, Jinsheng Chen^{1,2*}**

7 ¹Center for Excellence in Regional Atmospheric Environment, Institute of Urban Environment, Chinese Academy of Sciences,
8 Xiamen 361021, China

9 ²Key Lab of Urban Environment and Health, Institute of Urban Environment, Chinese Academy of Sciences, Xiamen 361021,
10 China

11 ³Fujian Provincial Key Laboratory of Pollution Monitoring and Control, Minnan Normal University, Zhangzhou, 363000,
12 China

13 ⁴Fujian Provincial Key Laboratory of Modern Analytical Science and Separation Technology, Minnan Normal University,
14 Zhangzhou, 363000, China

15 ⁵Key Laboratory of Environment Optics and Technology, Anhui Institute of Optics and Fine Mechanics, Chinese Academy of
16 Sciences, Hefei, 230031, China

17 ⁶University of Chinese Academy of Sciences, Beijing 100086, China

18 ⁷School of Environmental Science and Optoelectronic Technology, University of Science and Technology of China, Hefei,
19 230026, China

20 #These authors contributed equally to this work.

21 *Correspondence to:* Jinsheng Chen (jschen@iue.ac.cn) &Min Qin (mqin@aiofm.ac.cn)

22

23 **Abstract.** Because nitrous acid (HONO) photolysis is a key source of hydroxyl (OH) radicals, identifying the atmospheric
24 sources of HONO is essential to enhance the understanding of atmospheric chemistry processes and improve the accuracy of
25 simulation models. We performed seasonal field observations of HONO in a coastal city of southeastern China, along with
26 measurements of trace gases, aerosol compositions, photolysis rate constants (J), and meteorological parameters. The results
27 showed that the average observed concentration of HONO was 0.54 ± 0.47 ppb. Vehicle exhaust emissions contributed an
28 average of 1.45 % to HONO, higher than the values found in most other studies, suggesting an influence from diesel vehicle
29 emissions. The mean conversion frequency of NO_2 to HONO in the nighttime was the highest in summer due to water droplets

30 was evaporated under the condition of high temperatures. Based on a budget analysis, the rate of emission from unknown
31 sources (R_{unknown}) was highest around midday, with values of $4.51 \text{ ppb}\cdot\text{h}^{-1}$ in summer, $3.51 \text{ ppb}\cdot\text{h}^{-1}$ in spring, $3.28 \text{ ppb}\cdot\text{h}^{-1}$ in
32 autumn, and $2.08 \text{ ppb}\cdot\text{h}^{-1}$ in winter. Unknown sources made up the largest proportion of all sources in summer (81.25 %),
33 autumn (73.99 %), spring (70.87 %), and winter (59.28 %). The photolysis of particulate nitrate was probably a source in
34 spring and summer while the conversion from NO_2 to HONO on BC enhanced by light was perhaps a source in autumn and
35 winter. The variation of HONO at night can be exactly simulated based on the HONO/ NO_x ratio, while the $J(\text{NO}_3^-)_R \times \text{pNO}_3^-$
36 should be considered for daytime simulations in summer and autumn, or $1/4 \times (J(\text{NO}_3^-)_R \times \text{pNO}_3^-)$ in spring and winter.
37 Compared with O_3 photolysis, HONO photolysis has long been an important source of OH except for summer afternoon.
38 Observation on HONO across four seasons with various auxiliary parameters improves the comprehension of HONO
39 chemistry in southeastern coastal China.

40 **1 Introduction**

41 Nitrous acid (HONO) photolysis produces hydroxyl radical (OH), an important oxidant, in the troposphere (Zhou et al., 2011).
42 OH plays an important role in triggering the oxidation of volatile organic compounds and therefore determine the fate of many
43 anthropogenic atmospheric pollutants (Lei et al., 2018). Recent research results have shown that HONO production is the
44 cause of an increase in secondary pollutants (Li et al., 2010; Gil et al., 2019; Fu et al., 2019). Though extensive studies have
45 been conducted in the four decades since the first clear measurement of HONO (Perner and Platt, 1979), the HONO formation
46 mechanisms are still elusive, especially during the daytime, when there is a large difference between measured concentrations
47 and those calculated from known gas-phase chemistry (Sörgel et al., 2011). Identification of the sources of atmospheric HONO
48 and exploration of its formation mechanisms are beneficial for enhancing our comprehension of atmospheric chemistry
49 processes and improving the accuracy of atmospheric simulation models.

50 Commonly accepted HONO sources include direct emission from motor vehicles (Chang et al., 2016; Kirchstetter et al., 1996;
51 Kramer et al., 2020; Xu et al., 2015) or soil (Su et al., 2011; Tang et al., 2019; Oswald et al., 2013), the homogeneous
52 conversion of NO by OH (Seinfeld and Pandis, 1998; Kleffmann, 2007), and the heterogeneous reaction of NO_2 on humid
53 surfaces (Alicke, 2002; Finlayson-Pitts et al., 2003). Other homogeneous sources include nucleation reaction of NH_3 , NO_2 ,
54 and H_2O (Zhang and Tao, 2010), electronically excited H_2O and NO_2 for the production of HONO (Li et al., 2008), the
55 $\text{HO}_2\cdot\text{H}_2\text{O}$ complex and NO_2 for the production of HONO (Li et al., 2014). Other heterogeneous sources, include NO_2 reduced
56 on soot to produce HONO and drastically enhanced by light (Ammann et al., 1998; Monge et al., 2010), semivolatile organics
57 from diesel exhaust for the production of HONO (Gutzwiller et al., 2002), photoactivated of NO_2 on humic acid (Stemmler et
58 al., 2006), TiO_2 (Ndour et al., 2008), solid organic compounds (George et al., 2005), the photolysis of particulate nitrate by
59 ultraviolet (UV) light (Kasibhatla et al., 2018; Romer et al., 2018; Ye et al., 2017; Scharko et al., 2014), dissolution of NO_2
60 catalyzed by anion on aqueous microdroplets (Yabushita et al., 2009), the process of acid displacement (Vandenboer et al.,
61 2014), the conversion of NO_2 to HONO on the ground (Wong et al., 2011), NH_3 enhancing the heterogeneous reaction of NO_2

62 with SO₂ for the production of HONO (Ge et al., 2019), NH₃ promoting NO₂ dimers hydrolysis for HONO production through
63 stabilizing the state of product and reducing the reaction free energy barrier (Li et al., 2018b; Xu et al., 2019), heterogeneous
64 formation of HONO catalyzed by CO₂ (Xia et al., 2021). Heterogeneous processes are the most poorly understood, yet are
65 widely considered the main sources of HONO in previous studies. The uptake coefficients of NO₂ conversion to HONO on
66 surfaces (including aerosol, ground, buildings, and vegetation) vary from 10⁻⁹ to 10⁻² derived from different experiments
67 (Ammann et al., 1998; Kirchner et al., 2000; Underwood et al., 2001; Aubin and Abbatt, 2007; Zhou et al., 2015; Liu et al.,
68 2014; Vandenboer et al., 2013). It is still a challenge to extrapolate laboratory results to real surfaces. It is still under exploration
69 to distinguish the key step to determine the NO₂ uptake, and we are also not sure what role does radiation play in it. Absence
70 of major HONO sources during the daytime is another active ongoing research.

71 According to an analysis of 15 sets of field observations around the world (Elshorbany et al., 2012), the HONO/NO_x ratio
72 (0.02) predicts well HONO concentrations under different atmospheric conditions. To avoid underestimation of HONO in this
73 study, an empirical parameterization was applied to estimating the HONO concentration, because the current understanding
74 of HONO formation mechanisms is incomplete. Field measurements of HONO and its precursor NO₂ at sites with different
75 aerosol load & composition, photolysis rate constants, and meteorological parameters are necessary to deepen our knowledge
76 of the HONO formation mechanisms. Such measurements have been carried out in coastal cities in China, including
77 Guangzhou (Qin et al., 2009), Hong Kong (Xu et al., 2015), and Shanghai (Cui et al., 2018), where the air pollution is relatively
78 severe during their research period. However, there has been a lack of research into HONO in coastal cities with good air
79 quality, low concentrations of PM_{2.5}, but strong sunlight and high humidity. Insufficient research on coastal cities with good
80 air quality has resulted in certain obstacles to assessing the photochemical processes in these areas. Due to different emission-
81 source intensities and ground surfaces, the atmospheric chemistry of HONO in the southeastern coastal area of China is
82 predicted to have different pollution characteristics from those found in other coastal cities. Furthermore, HONO contributes
83 to the atmospheric photochemistry differently depending on the season (Li et al., 2010). Therefore, observations of atmospheric
84 HONO across different seasons in the southeastern coastal area of China are urgently needed.

85 Incoherent broadband cavity-enhanced absorption spectroscopy (IBBCEAS) was employed in this study to determine HONO
86 concentrations in the southeastern coastal city of Xiamen in August (summer), October (autumn), and December (winter) 2018
87 and March (spring) 2019. In addition, a series of other relevant trace gases, meteorological parameters, and photolysis rate
88 constants were measured at the same time to provide supplementary information to reveal the HONO formation mechanisms.
89 The main purposes of this study were to (1) calculate the values of unknown HONO daytime sources, (2) analyze the processes
90 leading to HONO formation, (3) simulate HONO concentrations based on an empirical parameterization, and (4) evaluate OH
91 production from HONO from 07:00 to 16:00 local time. These results were compared between the seasons.

92 **2 Methodology**

93 **2.1 Site description**

94 Our field observations were carried out ~80 m above the ground at a supersite located on the top of the Administrative Building
95 of the Institute of Urban Environment (IUE), Chinese Academy of Sciences (118°04'13"E, 24°36'52"N) in Xiamen, China in
96 August, October, and December 2018, and March 2019 (Fig. 1). The supersite was equipped with a complete set of
97 measurement tools, including those for measuring gases and aerosol species composition, meteorology parameters, and
98 photolysis rate constants, which provided a good chance to study the atmospheric chemistry of HONO in a coastal city of
99 southeastern China. As shown in Fig. 1 (left), Xiamen is located at the southeast coastal area of China and faces the Taiwan
100 Strait in the east. It suffers from sea and land breeze throughout the year with spring and summer more frequently (Xun et al.,
101 2017). The IUE supersite is surrounded by a Xinglin Bay, several universities (or institutes), and several major roads with
102 large traffic fleet, such as Jimei Road, Shenhai Expressway (870 m) and Xiasha Expressway (2300 m) (Fig. 1 (right)). The
103 area of Xiamen is 1700.61 km² with a population of 4.11 million (<http://tjj.xm.gov.cn/tjzl/>). The number of motor vehicles in
104 2018 was 1,572,088, which was 2.73 times as many as ten years ago. The surrounding soil is used for landscape greening not
105 for agricultural production.

106 **2.2 Instrumentation**

107 The atmospheric concentrations of both HONO and NO₂ were determined using IBBCEAS, which has previously been widely
108 applied to such measurements (Tang et al., 2019; Duan et al., 2018; Min et al., 2016). The IBBCEAS instrument was
109 customized by the Anhui Institute of Optics and Fine Mechanic (AIOFM), Chinese Academy of Sciences (Duan et al., 2018).
110 The resonant cavity is composed of a pair of high reflective mirrors separated by 70 cm and their reflectivity is approximately
111 0.99983 at 368.2 nm. The surface of the mirrors was purged by dry nitrogen at 0.1 Standard Liter per Minute (SLM), and the
112 air flow was controlled by mass flow controller to prevent the surface of the mirror from being contaminated. Light was
113 introduced into the resonant cavity and was emitted by a single light-emitting diode (LED) with full width at half maximum
114 (FWHM) of 13 nm, peak wavelength of 365 nm. Light transmitted through the cavity was received by a spectrometer
115 (QE65000, Ocean Optics Inc., USA) through an optical fiber with 600 μm diameter and a 0.22 numerical aperture.

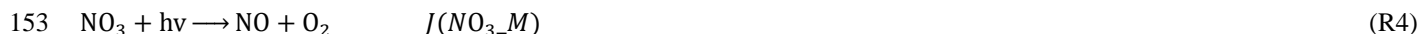
116 In order to avoid the drift of the center wavelength of the LED, the temperature of the LED was controlled to be approximately
117 25 ± 0.01 °C by using a thermoelectric cooler unit. In order to prevent particulate matter from entering the cavity and reducing
118 the effect of particulate matter on the effective absorption path, a 1 μm polytetrafluoroethylene (PTFE) filter membrane (Tisch
119 Scientific) was used in the front end of the sampling port. In order to ensure the quality of the data, the 1 μm PTFE filter
120 membrane was usually replaced once every three days and the sampling tube was thoroughly cleaned with alcohol once a
121 month. We increased the replacement frequency of the filter membrane and the cleaning frequency of the sampling tube in the
122 event of heavy pollution to ensure that the filter membrane and sampling tube are in a clean state. The length of sampling tube

123 with 6 mm outer diameter was approximately 3 m, the material was PFA with excellent chemical inertness and the sampling
 124 flow rate was 6 SLM meaning that the residence time of the gas in the sampling tube was less than 0.5 s. Besides, the sampling
 125 loss was calibrated before the experiment. We assessed the measured spectrum every day to ensure the authenticity of the
 126 measurement results. Multiple reflections in the resonator cavity enhanced the length of the effective absorption path, thereby
 127 enhancing the detection sensitivity of the instrument. The 1σ detection limits for HONO and NO_2 were about 60 ppt and
 128 100 ppt, respectively, and the time resolution was 1 min. The fitting wavelength range was selected as 359–387 nm. The
 129 measurement error of HONO of IBBCEAS was estimated to be about 9 %, considering both HONO secondary formation and
 130 sample loss. The sampling tube was heated to 35°C and covered by insulation cotton materials to prevent the effect of
 131 condensation of the water vapor (Lee et al., 2013).

132 The inorganic composition of $\text{PM}_{2.5}$ aerosols (SO_4^{2-} , NO_3^- , Cl^- , Na^+ , NH_4^+ , K^+ , Ca^{2+} , and Mg^{2+}) and concentrations of gases
 133 (HONO, HNO_3 , HCl, SO_2 , NH_3) were determined using a Monitor for Aerosols and Gases in ambient Air (MARGA, Model
 134 ADI 2080, Applikon Analytical B.V., the Netherlands). Ambient air was drawn into the sample box by a $\text{PM}_{2.5}$ cyclone (Teflon
 135 coated, URG-2000-30ENB) at the flow rate of $1 \text{ m}^3 \cdot \text{h}^{-1}$. Air sample was drawn firstly through the Wet Rotating Denuder (WRD)
 136 where gases diffused to the solution, and then particles were collected by a Steam Jet Aerosol Collector (SJAC). Absorption
 137 solutions were drawn from the SJAC and the WRD to syringes (25 ml). Samples were injected to Metrohm cation (500 μl
 138 loop) and anion (250 μl loop) chromatographs with the internal standard (LiBr) for 15 min after an hour when the syringes had
 139 been filled (Makkonen et al., 2012). Specific descriptions of the SJAC can be found in previous reports (Slanina et al., 2001;
 140 Wyers et al., 1993). Therefore, the times needed for the sampling period and the latter IC analysis on the MARGA system are
 141 a full hour and 15 minutes, respectively. The value measured in this hour is actual the concentration sampled in the previous
 142 hour, so the time corresponding to the sampling is matched with other instrument parameters (i.e., HONO, NO_x , J values).

143 Photolysis frequencies were determined using a photolysis spectrometer (PFS-100, Focused Photonics Inc., Hangzhou, China).
 144 These were calculated by multiplying the actinic flux F , quantum yield $\phi(\lambda)$ and the known absorption cross section $\sigma(\phi)$. The
 145 measurements included the photolysis rate constants $J(\text{O}^1\text{D})$, $J(\text{HCHO_M})$, $J(\text{HCHO_R})$, $J(\text{NO}_2)$, $J(\text{H}_2\text{O}_2)$, $J(\text{HONO})$, J
 146 (NO_3_M) and $J(\text{NO}_3_R)$, and the spectral band ranged from 270 to 790 nm. Hemispherical (2π sr) angular response deviations
 147 were within ± 5 %. The photolysis rate constants with $_R$ and $_M$ represented radical photolysis channel and molecular
 148 photolysis channel, respectively. Specifically, HCHO was removed by the reactions (R1) and (R2), and NO_3 was removed by
 149 the reactions R(3) and R(4), respectively (Röckmann et al., 2010).





154 The O_3 concentration was determined by ultraviolet photometric analyzer [Model 49i, Thermo Environmental Instruments
155 (TEI) Inc.], and the limit of the instrument is 1.0 ppb. The NO concentration was determined by a chemiluminescence analyzer
156 (TEI model 42i) with a molybdenum converter. The detection limit and the uncertainty of the TEI model 42i were 0.5 ppb and
157 10 %, respectively. Although the TEI model 42i also measures the concentration of NO_2 , this value might actually include
158 other active nitrogen components (Villena et al., 2012). As expected, the NO_2 concentration measured by IBBCEAS had the
159 same trend as the NO_2 measured by TEI 42i, and NO_2 concentration measured by IBBCEAS was always lower than that by
160 TEI 42i (Fig. S1). Therefore, the NO_2 concentration as measured by IBBCEAS was used in this study. An oscillating
161 microbalance with a tapered element was applied to determine the $\text{PM}_{2.5}$ concentration with uncertainty of 10-20 %. Black
162 carbon (BC) was measured by aethalometer at 7 wavelengths (in using 880 nm wavelength). When the tape was < 10 %,
163 aethalometer fiber tape was replaced. Meteorological parameters were determined by an ultrasonic anemometer (150WX,
164 Airmar, USA). The time resolution of all instruments was unified to 1 h to facilitate comparison. Ultraviolet radiation (UV)
165 was determined by a UV radiometer (KIPP & ZONEN, SUV5 Smart UV Radiometer).

166 **3 Results and discussion**

167 **3.1 Overview of data**

168 Fig. 2 showed an overview of the determined HONO, NO, NO_2 , $\text{PM}_{2.5}$, NO_3^- , BC, $J(\text{HONO})$, temperature (T) and relative
169 humidity (RH) in this study. The entire campaign was characterized by subtropical monsoon climate with high temperature
170 (9.82–34.42 °C) and high humidity (29.24–100 %). The mean values (\pm standard deviation) of temperature and relative
171 humidity were 22.24 ± 5.41 °C and 78.35 ± 14.07 %, respectively. Elevated concentrations of NO_x , i.e., up to 156.17 ppb of
172 NO, and 172.42 ppb of NO_2 , were observed, possibly due to dense vehicle emissions near this site. The photolysis rate constants
173 $J(\text{O}^1\text{D})$, $J(\text{HCHO_M})$, $J(\text{HCHO_R})$, $J(\text{NO}_2)$, $J(\text{H}_2\text{O}_2)$, $J(\text{HONO})$, $J(\text{NO}_3_M)$ and $J(\text{NO}_3_R)$ had the same temporal variation
174 (Fig. S2), although their orders of magnitude were different. The correlation coefficients between $J(\text{HONO})$ and other
175 photolysis rate constants were above 0.965 (not shown). Both $J(\text{HONO})$ and UV peaked around noon, and the maximum of
176 $J(\text{HONO})$ ($2.02 \times 10^{-3} \text{ s}^{-1}$) and UV ($55.62 \text{ W}\cdot\text{m}^{-2}$) appeared at 13:00 on 11 March 2019, and 12:00 on 14 August 2018,
177 respectively. This area was dominated by photochemical pollution, while particulate pollution was relatively light. No haze
178 episodes occurred across four seasons with 111 days because daily mass concentration of $\text{PM}_{2.5}$ was lower than the National
179 Ambient Air Quality Standard (Class II: $75 \mu\text{g}\cdot\text{m}^{-3}$). For O_3 , 10 episodes occurred with eight-hour maximum concentrations
180 of O_3 exceeding the Class II: $160 \mu\text{g}\cdot\text{m}^{-3}$. Maximum mixing ratio of O_3 was 113.81 ppb, occurring in the afternoon with strong
181 ultraviolet radiation ($42.72 \text{ W}\cdot\text{m}^{-2}$) and low NO concentration (0.75 ppb) titrating O_3 . In general, the level of pollutants in this
182 area was relatively low. Campaign-averaged levels of NO_2 , NO, NO_3^- , $\text{PM}_{2.5}$, O_3 , and BC were 14.99 ± 8.93 ppb, 5.80 ± 11.98

183 ppb, $5.59 \pm 6.26 \mu\text{g}\cdot\text{m}^{-3}$, $27.78 \pm 17.95 \mu\text{g}\cdot\text{m}^{-3}$, 28.29 ± 21.14 ppb, and $1.67 \pm 0.97 \mu\text{g}\cdot\text{m}^{-3}$, respectively. The maximum value
184 of HONO (3.51 ppb) appeared at 08:00 on 4 December 2018. The high value of HONO was always accompanied by relative
185 high values of NO and NO₂ or PM_{2.5}, BC and NO₃⁻. The average measured ambient HONO concentration at the measurement
186 site for all measurement periods was 0.54 ± 0.47 ppb. The HONO concentration measured at this site was comparable to those
187 measured at other suburban sites (Liu et al., 2019a; Xu et al., 2015; Nie et al., 2015; Park et al., 2004), was obvious lower than
188 those measured at urban sites and industrial site (Li et al., 2018a; Yu et al., 2009; Hou et al., 2016; Qin et al., 2009; Wang et
189 al., 2013; Shi et al., 2020; Spataro et al., 2013; Huang et al., 2017; Wang et al., 2017), and was obvious higher than those
190 measured at marine background(Wen et al., 2019), Marine boundary layer(Ye et al., 2016), and coastal remote (Meusel et al.,
191 2016) , as shown in Table S1.

192 As shown in Table 1, in the daytime (06:00–18:00, including 06:00, local time (LT)), the highest concentration of HONO was
193 found in spring and summer (0.72 ppb), followed by winter (0.61 ppb) and autumn (0.50 ppb). In short, the seasonal variation
194 of HONO was well correlated with the seasonality of RH, with high RH in spring (84.21 %) and summer (84.12 %), followed
195 by winter (78.13 %) and autumn (69.55 %). In conditions of low RH, the adsorption rate of NO₂ is not as rapid as that of
196 HONO, resulting in a reduction in the conversion rate of NO₂ to HONO and thus a reduction in the concentration of HONO
197 (Stutz et al., 2004). This seasonal variation in HONO concentration was different from those measured in Jinan (Li et al.,
198 2018a), Nanjing(Liu et al., 2019a), and Hong Kong (Xu et al., 2015). The elevated HONO concentrations in summer, when
199 there is strong solar radiation, suggests the existence of strong sources of HONO and its important contribution to the
200 production of OH radicals. Interestingly, the HONO concentration in the nighttime was lower than that in the daytime in all
201 four seasons. Similar results were found in Hong Kong, which is also a coastal city (Xu et al., 2015). However, most previous
202 studies have found that the HONO concentration at night is significantly higher than that during the day (Wang et al., 2015;
203 Liu et al., 2019a; Li et al., 2018a; Elshorbany et al., 2009; Acker et al., 2006; Yu et al., 2009). The higher HONO in the daytime
204 is likely due to the higher NO_x or nitrate photolysis as discussed in following section.

205 The ratio of HONO to NO_x or the ratio of HONO to NO₂ have been extensively applied to indicate heterogeneous conversion
206 of NO₂ to HONO (Li et al., 2012; Liu et al., 2019a; Zheng et al., 2020). Compared with the HONO/NO₂ ratio, the HONO/NO_x
207 ratio can better avoid the influence of primary emissions (Liu et al., 2019a). In this study, the HONO/NO_x ratios during the
208 day were higher than those during the night, indicating that light promotes the conversion of NO_x to HONO. The highest
209 daytime HONO/NO_x ratio was found in summer (0.072), followed in turn by autumn (0.048), spring (0.034), and winter (0.023).
210 The elevated HONO/NO_x ratio in summer indicates a greater net HONO production (Xu et al., 2015). The low HONO/NO_x
211 ratio in winter can probably be ascribed to heavy emissions and high concentrations of NO in winter (Table 1). The HONO/NO_x
212 ratios during every season in Xiamen were in general higher than those found in studies of other cities, which indicates greater
213 net HONO production in Xiamen.

214 The diurnal patterns of HONO, NO_x, HONO/NO_x, and $J(\text{NO}_2)$ averaged for every hour in each season are shown in Fig. 3. As
215 shown in Fig. 3a, the HONO concentration had similar diurnal variation patterns across the four seasons. The maximum values

216 of the HONO concentration were 1.12 ppb in winter, 1.03 ppb in summer, 0.98 ppb in spring, and 0.65 ppb in autumn, and
217 these occurred in the morning rush hour (07:00–08:00), which indicates that direct vehicle emissions may be a significant
218 source of HONO. The contribution of direct vehicle emissions to HONO will be quantified in Sect. 3.2. The HONO
219 concentration reduced rapidly from the morning rush hour to sunset, and this was caused by rapid photolysis combined with
220 increased height of the boundary layer. The minimum values of HONO concentration were 0.47 ppb in spring, 0.23 ppb in
221 winter, 0.21 ppb in summer, and 0.14 ppb in autumn, and these appeared at sunset, between 16:00 and 18:00. The HONO
222 concentration increased gradually after sunset, which indicates that release from HONO sources exceeded its dry deposition
223 (Wang et al., 2017). There was a slight difference in the diurnal variation of HONO between autumn and the other seasons. A
224 rapid reduction of HONO after the morning rush hour was found in spring, summer, and winter. In comparison, the HONO in
225 autumn had an almost constant concentration between 07:00 and 11:00 because NO_x decreased slowly during this period.

226 As shown in Fig. 3b, NO_x concentration followed an expected profile in the four seasons, with peaks of 45.58 ppb in winter,
227 40.47 ppb in spring, 32.47 ppb in summer, and 20.07 ppb in autumn, each occurring in the morning rush hour at 10:00, 09:00,
228 08:00, and 07:00 local time, respectively. After these peaks, NO_x decreased during the day in each season, probably due to
229 photochemical transformation and increasing boundary-layer depth. The NO_x concentrations then began to rise from their
230 minima of 8.20 ppb in summer, 8.85 ppb in autumn, 18.10 ppb in winter, and 23.09 ppb in spring after 14:00, 13:00, 15:00,
231 and 16:00 local time, respectively, which was caused by a combination of weak photochemical transformation and reduction
232 in the boundary-layer depth. The NO_x concentrations during winter and spring were significantly higher than those during
233 autumn and summer. Both the maxima and minima of NO_x appeared later in spring and winter compared with summer and
234 autumn.

235 It is possible to better describe the behavior of HONO using the HONO/NO_x ratio. The higher HONO/NO_x ratio found at noon
236 in the different seasons, especially in summer and autumn (Fig. 3c), indicates an additional daytime HONO source(Liu et al.,
237 2019a; Xu et al., 2015). It is worth noting that the maximum value of this ratio in summer (0.147) was significantly higher
238 than the maximum in other seasons, especially in winter (0.034). Fig. 3d shows that the value of the HONO/NO_x ratio increased
239 with the photolysis rate constant of NO₂ in summer and autumn, suggesting that the additional HONO source is probably
240 correlated with light (Xu et al., 2015; Wang et al., 2017; Li et al., 2018a; Li et al., 2012). The increase in the HONO/NO₂ ratio
241 during the day can be seen more clearly in Fig. 4, and its high value indicates a high HONO production efficiency, which
242 cannot be ascribed to NO₂ conversion due to the weak correlation between HONO and NO₂ in summer. Furthermore, high
243 HONO/NO₂ ratios were accompanied by high *J*(NO₂) in summer, which indicates that HONO formation during the daytime
244 is more possible to relate to light rather than Reaction (R5).



246 However, the observed maxima can also be ascribed to sources independent from NO_x concentration, such as soil emissions
247 (Su et al., 2011) and photolysis of particulate nitrate (Zhou et al., 2011; Ye et al., 2016), which are not influenced by the

248 decrease of NO_x concentration around noon. A more specific discussion of daytime HONO sources considering the photolysis
249 of particulate nitrate will be given in Sect. 3.4.3. The HONO emissions from soil were estimated to be 2–5 ppb h⁻¹ (Su et al.,
250 2011). However, soil emission was a negligible source of HONO in this study since the surrounding soil is not used for
251 agriculture, and this greatly reduces the amount of HONO released due to no fertilization process (Su et al., 2011).

252 3.2 Direct vehicle emission of HONO

253 The K⁺ levels were 0.26, 0.13, 0.14, and 0.24 μg·m⁻³ for spring, summer, autumn, and winter, respectively. The K⁺ levels
254 during the four seasons were lower than 2 μg·m⁻³, which indicated that biomass burning has little effect on this site (Xu et al.,
255 2019). Hence, only vehicle emissions were considered in this study. The consistent diurnal variations in HONO and NO_x
256 presented in Sect. 3.1 (Fig. 3) also indicate HONO emissions from local traffic. Five criteria were applied to choose cases that
257 guaranteed the presence of fresh plumes (Xu et al., 2015; Liu et al., 2019a): (1) UV < 10 W·m⁻²; (2) short-duration air masses
258 (<2 h); (3) HONO correlating well with NO_x ($R^2 > 0.60$, $P < 0.05$); (4) NO_x > 20 ppb (highest 25 % of NO_x value); and (5)
259 $\Delta\text{NO}/\Delta\text{NO}_x > 0.85$. A total of 23 cases met these strict criteria for estimation of the HONO vehicle emission ratios. The slopes
260 of scatter plots of HONO vs NO_x were used as the emission factors.

261 A total of 23 vehicle emission plumes were summarized in Table 2, and these were used for estimation of the vehicle emission
262 ratios. These plumes were considered to be truly fresh because the mean $\Delta\text{NO}/\Delta\text{NO}_x$ ratio (the linear slope of NO with NO_x)
263 of the selected air masses was 99 %. Vehicle plumes unavoidably mixing with other air masses resulted in the correlation
264 coefficients (R^2) between HONO and NO_x varying among the cases, and these ranged from 0.64 to 0.92. The obtained
265 $\Delta\text{HONO}/\Delta\text{NO}_x$ ratios (the linear slope of HONO with NO_x) ranged from 0.24 % to 2.95 %, with an average value ($\pm\text{SD}$) of
266 (1.45 ± 0.78) %. These $\Delta\text{HONO}/\Delta\text{NO}_x$ ratios have comparability to those obtained in Guangzhou (1.4 % (Qin et al., 2009);
267 1.8 % (Li et al., 2012)) and Houston (1.7 % (Rappenglück et al., 2013)), but are significantly higher than those measured in
268 Jinan (0.53 % (Li et al., 2018a)) and Santiago (0.8 % (Elshorbany et al., 2009)). The types of vehicle engine, the use of catalytic
269 converters, and different fuels will affect the vehicle emission factors (Kurtenbacha et al., 2001). A potential reason for the
270 relatively higher $\Delta\text{HONO}/\Delta\text{NO}_x$ values in our study is that heavy-duty diesel vehicles pass by on the surrounding highway
271 (Rappenglück et al., 2013). It is necessary to examine the specific vehicle emission factors in target cities because of these
272 differences in $\Delta\text{HONO}/\Delta\text{NO}_x$ ratios. Roughly assuming that NO_x mainly arises from vehicle emissions, a mean $\Delta\text{HONO}/\Delta\text{NO}_x$
273 value of 1.45 % was used as the emission factor in this study, and this value was adopted to estimate the contribution of vehicle
274 emissions P_{emis} to the HONO concentration using

$$275 P_{\text{emis}} = \text{NO}_x \times 0.0145. \quad (1)$$

276 We can then obtain the corrected HONO concentration ($\text{HONO}_{\text{corr}}$) for further analysis from the equation

$$277 \text{HONO}_{\text{corr}} = \text{HONO} - P_{\text{emis}}. \quad (2)$$

278 3.3 Nighttime heterogeneous conversion of NO₂ to HONO

279 3.3.1 Conversion rate of NO₂ to HONO

280 Nighttime HONO_{corr} concentrations can be estimated from the heterogeneous conversion reaction (Meusel et al., 2016; Alicke,
281 2002; Su et al., 2008a). Although the mechanism of the nighttime HONO heterogeneous reaction is unclear, the formula for
282 the heterogeneous conversion (C_{HONO}^0) of NO₂ to HONO can be expressed as

$$283 C_{\text{HONO}}^0 = \frac{[\text{HONO}_{\text{corr}}]_{t_2} - [\text{HONO}_{\text{corr}}]_{t_1}}{(t_2 - t_1) \times \overline{[\text{NO}_2]}}, \quad (3)$$

284 where $\overline{[\text{NO}_2]}$ is the mean value of NO₂ concentration between t_1 and t_2 . Eq. (4) has been suggested as a way to avoid the
285 interference of direct emissions and diffusion (Su et al., 2008a):

$$286 C_{\text{HONO}}^X = \frac{\left(\frac{[\text{HONO}_{\text{corr}}]_{(t_2)}}{[X]_{t_2}} - \frac{[\text{HONO}_{\text{corr}}]_{(t_1)}}{[X]_{(t_1)}} \right) \overline{[X]}}{(t_2 - t_1) \frac{1}{2} \left(\frac{[\text{NO}_2]_{(t_2)}}{[X]_{(t_2)}} + \frac{[\text{NO}_2]_{(t_1)}}{[X]_{(t_1)}} \right) \overline{[X]}} = \frac{2 \left(\frac{[\text{HONO}_{\text{corr}}]_{(t_2)}}{[X]_{t_2}} - \frac{[\text{HONO}_{\text{corr}}]_{(t_1)}}{[X]_{(t_1)}} \right)}{(t_2 - t_1) \left(\frac{[\text{NO}_2]_{(t_2)}}{[X]_{(t_2)}} + \frac{[\text{NO}_2]_{(t_1)}}{[X]_{(t_1)}} \right)}, \quad (4)$$

287 where $[\text{HONO}_{\text{corr}}]_t$, $[\text{NO}_2]_t$, and $[X]_t$ were the concentrations of HONO, NO₂, and species used for normalization (including
288 NO₂, CO, and black carbon (BC) in this study), respectively, at time t , $\overline{[X]}$ is the average concentration of reference species
289 between t_1 and t_2 , and C_{HONO}^X represents the conversion rate normalized against reference species X (Su et al., 2008a). There
290 were 86 cases meeting the criteria. Such a large number of cases contributes to the statistical analysis of the heterogeneity of
291 HONO formation. The average values of C_{HONO}^0 , $C_{\text{HONO}}^{\text{NO}_2}$, $C_{\text{HONO}}^{\text{CO}}$, and $C_{\text{HONO}}^{\text{BC}}$ were 0.48 % h⁻¹, 0.46 % h⁻¹, 0.46 % h⁻¹, and
292 0.46 % h⁻¹, respectively. The combined $C_{\text{HONO}}^{\text{C}}$ was 0.46 % h⁻¹. The average C_{HONO} values obtained using different
293 normalization methods agreed well. Therefore, an estimation value of 0.46 % h⁻¹ should be suitable for the nighttime
294 conversion rate from NO₂ to HONO.

295 We also compared the conversion rates calculated in this study with other experiments. As shown in Table 3, $C_{\text{HONO}}^{\text{C}}$ varied
296 widely, from 0.29 % h⁻¹ to 2.40 % h⁻¹, which may be due to the various kinds of land surface in the various environments. The
297 $C_{\text{HONO}}^{\text{C}}$ in Xiamen is comparable to those derived in Shanghai (0.70 % h⁻¹ (Wang et al., 2013)), Jinan (0.68 % h⁻¹ (Li et al.,
298 2018a)), and Hong Kong (0.52 % h⁻¹ (Xu et al., 2015)), less than the values calculated from most other sites, including Xinken
299 (1.60 % h⁻¹ (Su et al., 2008a)), Guangzhou (2.40 (Li et al., 2012)), Spain (1.50 (Sörgel et al., 2011)), Beijing (0.80 (Wang et
300 al., 2017)), the eastern Bohai Sea (1.80 % h⁻¹ (Wen et al., 2019)), and Kathmandu (1.40 % h⁻¹ (Yu et al., 2009)), but more than
301 the value obtained in Shandong (0.29 % h⁻¹ (Wang et al., 2015)). The highest $C_{\text{HONO}}^{\text{C}}$ was found in summer, with a value of
302 0.55 % h⁻¹, which will be explained in Sect. 3.3.2. Another study also found that the highest $C_{\text{HONO}}^{\text{C}}$ (1.00 % h⁻¹) appeared in
303 summer (Wang et al., 2017).

304 3.3.2 The influence factors on HONO formation

305 The hydrolysis of NO_2 on wet surfaces producing HONO is first-order affected by the concentration of NO_2 (Finlayson-Pitts
306 et al., 2003; Jenkin et al., 1988) and the absorption of water on the surfaces (Finlayson-Pitts et al., 2003; Kleffmann et al.,
307 1998). A scatter plot of $\text{HONO}_{\text{corr}}/\text{NO}_2$ vs RH is shown in Fig. 5. We calculated the top-five $\text{HONO}_{\text{corr}}/\text{NO}_2$ ratios in every 5 %
308 RH interval based on a method introduced in previous literature (Li et al., 2012; Stutz et al., 2004), which will reduce the
309 influence of those circumstances such as advection, the time of the night, and the surface density. These averaged maxima and
310 standard deviations are shown in Fig. 5 as orange squares, except where data were sparse in a particular 5 % RH interval.

311 As for autumn and winter, the influence of RH on $\text{HONO}_{\text{corr}}/\text{NO}_2$ can be divided into two parts. The RH promoted an increase
312 in $\text{HONO}_{\text{corr}}/\text{NO}_2$ for RH values less than 77.96 % in autumn and 91.99 % in winter, which is in line with the reaction kinetics
313 of Reaction (R5). However, RH inhibits the conversion of NO_2 to HONO when RH is higher than a turning point. According
314 to many previous studies, water droplets will be formed on the surface of the ground or of aerosols when RH exceeds a certain
315 value, thus resulting in a negative dependence of $\text{HONO}_{\text{corr}}/\text{NO}_2$ on RH (He et al., 2006; Zhou et al., 2007). A similar
316 phenomenon was also found in Guangzhou and in Shanghai (70 %, (Li et al., 2012; Wang et al., 2013)) and in Kathmandu and
317 in Beijing (65 %, (Yu et al., 2009; Wang et al., 2017)). However, in summer, RH appeared to promote the increase of
318 $\text{HONO}_{\text{corr}}/\text{NO}_2$ without a turning point, suggesting that HONO production at night in summer strongly depends on RH. Another
319 study also found a similar phenomenon in the summer in Guangzhou (Qin et al., 2009). This phenomenon might be caused by
320 water droplets being evaporated by high temperatures. This is the reason for the highest $C_{\text{HONO}}^{\text{C}}$ in summer. As for spring, the
321 relationship between $\text{HONO}_{\text{corr}}/\text{NO}_2$ and RH is very complicated and needs to be explored further in the future.

322 It has been found that NH_3 promoted hydrolysis of NO_2 and production of HONO and NH_4NO_3 (Xu et al., 2019; Li et al.,
323 2018b). The correlations between the $\text{HONO}_{\text{corr}}/\text{NO}_2$ ratio, the $\text{NO}_3^-/\text{NO}_2$ ratio and the NH_3 concentration in four seasons were
324 examined to investigate the influence of NH_3 on HONO formation through promoting hydrolysis of NO_2 . Only nighttime data
325 with RH above 80 % were chosen to avoid daytime rapid photolysis of HONO and enough water for NO_2 quick hydrolysis. (Xu
326 et al., 2019). As shown in Fig. 6, for summer, the correlations between NH_3 and $\text{HONO}_{\text{corr}}/\text{NO}_2$ ratio was very poor and even
327 negative ($R=-0.0438$), and the correlation between $\text{NO}_3^-/\text{NO}_2$ ratio and NH_3 was also negative (-0.2908). These results
328 indicated that NH_3 played a minor role in HONO production in summer. For autumn, although $\text{NO}_3^-/\text{NO}_2$ ratio correlated well
329 with NH_3 ($R=0.3965$) in autumn, $\text{HONO}_{\text{corr}}/\text{NO}_2$ ratio had negative correlation with NH_3 ($R=-0.1305$), which also indicated
330 that NH_3 played a minor role in HONO production in autumn. For spring, the correlation coefficient between the
331 $\text{HONO}_{\text{corr}}/\text{NO}_2$ ratio and the NH_3 concentration was highest among four seasons (0.3662), and the correlation between the
332 $\text{NO}_3^-/\text{NO}_2$ ratio and the NH_3 concentration was positive (0.1716). These phenomena proved that NH_3 might promote HONO
333 and NH_4NO_3 production through promoting NO_2 hydrolysis in spring. For winter, positive correlations were found in NH_3
334 with both HONO/NO_2 ratio ($R=0.1718$) and $\text{NO}_3^-/\text{NO}_2$ ratio ($R=0.2543$), which indicated that NH_3 might promote NO_2
335 hydrolysis and HONO production in winter. All in all, NH_3 might promote NO_2 hydrolysis and HONO production in spring
336 and winter, whereas NH_3 played a minor role in HONO production in summer and autumn.

337 As shown in Fig. S3, $\text{HONO}_{\text{corr}}/\text{NO}_2$ reached a pseudo-steady state from 03:00 to 06:00 LT every night. A correlation analysis
 338 of $\text{HONO}_{\text{corr}}/\text{NO}_2$ with $\text{PM}_{2.5}$ was carried out in the pseudo-steady state to understand the impact of aerosols on HONO
 339 production. Although we did not measure the aerosol surface density, the aerosol mass concentration can be used to replace
 340 this parameter (Huang et al., 2017; Park et al., 2004; Cui et al., 2018). The positive correlation of $\text{HONO}_{\text{corr}}$ with $\text{PM}_{2.5}$
 341 ($R_1 = 0.4987$) (Fig. 7a) may be a result of atmospheric physical processes such as convergence and diffusion. Using the
 342 $\text{HONO}_{\text{corr}}/\text{NO}_2$ ratio instead of a single HONO concentration for correlation analysis with $\text{PM}_{2.5}$ reduce the impact of physical
 343 processes and indicate the extent of conversion of NO_2 to HONO. Therefore, it was more credible that $\text{HONO}_{\text{corr}}/\text{NO}_2$ would
 344 be moderately positively correlated with $\text{PM}_{2.5}$ ($R_2 = 0.2331$) during the whole observation period (Fig. 7b). As denoted by
 345 larger green squares in the Fig. 7b, $\text{HONO}_{\text{corr}}/\text{NO}_2$ correlated well with $\text{PM}_{2.5}$ when its concentration was higher than $35 \mu\text{g}\cdot\text{m}^{-3}$
 346 ($R_3 = 0.4568$). The larger the amount of HONO produced by the heterogeneous reaction of NO_2 on the aerosol surface, the
 347 better the correlation between HONO/NO_2 and $\text{PM}_{2.5}$ (Cui et al., 2018; Wang, 2003; Hou et al., 2016; Li et al., 2012; Nie et
 348 al., 2015).

349 3.4 Daytime sources of HONO

350 3.4.1 Budget analysis of HONO

351 Having discussed the nighttime chemical behavior of HONO, we now concentrate on the daytime chemical behavior of HONO.
 352 Here, R_{unknown} is used to stand for the rate of emission from unknown sources. The value of R_{unknown} was estimated based on
 353 the balance between sources and sinks due to its short atmospheric lifetime. The sources are: (1) oxidation of NO by OH
 354 ($R_{\text{OH+NO}} = k_{\text{OH+NO}}[\text{NO}][\text{OH}]$), (2) dark heterogeneous production (P_{het}), and (3) direct vehicle emission (P_{emis}); the sinks
 355 are (1) HONO photolysis ($R_{\text{phot}} = J_{\text{HONO}}[\text{HONO}]$), (2) oxidation of HONO by OH ($R_{\text{OH+HONO}} = k_{\text{OH+HONO}}[\text{HONO}][\text{OH}]$),
 356 and (3) dry deposition (L_{dep}). The value of R_{unknown} can then be calculated according to

$$357 R_{\text{unknown}} = J_{\text{HONO}}[\text{HONO}] + k_{\text{OH+HONO}}[\text{HONO}][\text{OH}] + L_{\text{dep}} + \frac{\Delta[\text{HONO}]}{\Delta t} - k_{\text{OH+NO}}[\text{NO}][\text{OH}] - P_{\text{het}} - P_{\text{emis}}, \quad (5)$$

358 Where $k_{\text{OH+HONO}} = 6.0 \times 10^{-12} \text{ cm}^3 \text{ molecules}^{-1} \text{ s}^{-1}$ and $k_{\text{OH+NO}} = 7.4 \times 10^{-12} \text{ cm}^3 \text{ molecules}^{-1} \text{ s}^{-1}$, values cited from a previous
 359 study (Sörgel et al., 2011). The OH concentration ($[\text{OH}]$) was estimated in this study because no data for this value were
 360 available. An improved empirical formula, Eq. (6), was applied to estimate $[\text{OH}]$ using the NO_2 and HONO concentrations
 361 and the photolysis rate constants (J) of NO_2 , O_3 , and HONO (Wen et al., 2019). Eq. (6) fully considers the influence of
 362 photolysis and precursors on the concentration of $[\text{OH}]$.

$$363 [\text{OH}] = 4.1 \times 10^9 \times \frac{J(O^1D)^{0.83} \times J(\text{NO}_2)^{0.19} \times (140 \times \text{NO}_2 + 1) + \text{HONO} \times J(\text{HONO})}{0.41 \times \text{NO}_2^2 + 1.7 \times \text{NO}_2 + 1 + \text{NO} \times k_{\text{NO+OH}} + \text{HONO} \times k_{\text{HONO+OH}}} \quad (6)$$

364 During spring, summer, autumn, and winter, the average midday OH concentrations were $8.86 \times 10^6 \text{ cm}^{-3}$, $1.48 \times 10^7 \text{ cm}^{-3}$,
 365 $1.36 \times 10^7 \text{ cm}^{-3}$, and $6.19 \times 10^6 \text{ cm}^{-3}$, respectively, which were within the range of those obtained in other studies varying from
 366 $4 \times 10^6 \text{ cm}^{-3}$ to $1.7 \times 10^7 \text{ cm}^{-3}$ (Tan et al., 2017; Lu et al., 2013).

367 $\frac{\Delta[\text{HONO}]}{\Delta t}$ is the observed change of HONO concentration ($\text{ppb}\cdot\text{s}^{-1}$). The value of $\frac{\Delta[\text{HONO}]}{\Delta t}$ is the concentration difference between
368 the center of one interval (1 min) and the center of the next interval, and this accounts for changes in concentration levels
369 (Sörgel et al., 2011). The parameter L_{dep} can be quantified by multiplying the dry deposition rate of HONO by the observed
370 HONO concentration and then dividing by the mixing layer height ($L_{\text{dep}} = \frac{v_{\text{HONO}}^{\text{ground}} \times [\text{HONO}]}{H}$). A value of $v_{\text{HONO}}^{\text{ground}} = 2 \text{ cm}\cdot\text{s}^{-1}$ was
371 used for the deposition rate (Sörgel et al., 2011; Su et al., 2008a). Although the mixing layer heights during spring, summer,
372 autumn, and winter were 1074.4 m, 1173.8 m, 1494.6 m, and 1310.4 m, respectively (Gao, 1999), most of HONO can not
373 reach the height of 200 m due to rapid photolysis of HONO during the daytime. Therefore, the mixing layer height 200 m was
374 used to parameterize L_{dep} . In summarizing the known HONO sources, we included the nighttime heterogeneous production as
375 a known source based on the assumption that the day continues in the same way as the night (Sörgel et al., 2011). The term
376 P_{hete} was parameterized by NO_2 conversion at night using the formula $P_{\text{hete}} = C_{\text{HONO}}^{\text{C}}[\text{NO}_2]$ (Alicke, 2002).

377 Fig. 8 shows the contributions of each term in Eq. (7) to the HONO budgets in different seasons. Photolysis of HONO (R_{phot})
378 formed the largest proportion of the sinks in all four seasons, accounting for 87.85 %, 88.79 %, 88.15 %, and 86.71 % in spring,
379 summer, autumn, and winter, respectively. The value of R_{phot} in summer was the highest ($3.60 \text{ ppb}\cdot\text{h}^{-1}$), followed by spring
380 ($3.08 \text{ ppb}\cdot\text{h}^{-1}$), autumn ($2.38 \text{ ppb}\cdot\text{h}^{-1}$) and winter ($2.26 \text{ ppb}\cdot\text{h}^{-1}$). The oxidation of HONO by OH contributed little to HONO
381 sinks (2.77 % of all sinks). Dry deposition (L_{dep}) was also very small (9.35 % of all sinks). As for known sources, $R_{\text{OH+NO}}$ was
382 the main known source in all four seasons, wherein the largest proportion was found in summer (64.44 %), followed by autumn
383 (53.66 %), spring (53.25 %), and winter (51.73 %). Direct emission was second among the known sources, accounting for
384 38.36 %, 27.49 %, 37.02 %, and 40.81 % in spring, summer, autumn, and winter, respectively. Dark heterogeneous formation
385 (P_{hete}) was almost negligible in the daytime, accounting for approximately 8.31 % of known sources during the whole
386 observation period. As for unknown sources, these made up the largest proportion of all sources found in summer (81.25 %),
387 followed by autumn (73.99 %), spring (70.87 %) and winter (59.28 %).

388 It is worth noting that R_{unknown} exhibited a maximum around noon in all seasons. A previous study in Wangdu (Liu et al., 2019b)
389 also found that unknown sources of HONO reached a maximum at midday, with the strongest photolysis rates in summer. This
390 strengthens the validity of the assumption that the missing HONO formation mechanism is related to a photolytic source
391 (Michoud et al., 2014). In the present study, the daily maximum R_{unknown} value was $4.51 \text{ ppb}\cdot\text{h}^{-1}$ in summer, followed by
392 $3.51 \text{ ppb}\cdot\text{h}^{-1}$ in spring, $3.28 \text{ ppb}\cdot\text{h}^{-1}$ in autumn and $2.08 \text{ ppb}\cdot\text{h}^{-1}$ in winter. Average R_{unknown} during the whole observation was
393 $2.32 \text{ ppb}\cdot\text{h}^{-1}$, which was almost at the upper-middle level of studies reported: $0.5 \text{ ppb}\cdot\text{h}^{-1}$ in a forest near Jülich,
394 Germany (Kleffmann, 2005); $0.77 \text{ ppb}\cdot\text{h}^{-1}$ at a rural site in the Pearl River delta, China (Li et al., 2012); $1.04 \text{ ppb}\cdot\text{h}^{-1}$ at a
395 suburban site in Nanjing, China (Liu et al., 2019a); $\approx 2 \text{ ppb}\cdot\text{h}^{-1}$ in Xinken, China (Su et al., 2008a); and $2.95 \text{ ppb}\cdot\text{h}^{-1}$ in the urban
396 atmosphere of Jinan, China (Li et al., 2018a).

397 3.4.2 Exploration of possible unknown daytime sources

398 According to the analyses in Sect. 3.1 and Sect. 3.4.1, the unknown sources are likely to be related to light. It was indeed found
 399 that the unknown sources have a good correlation with the parameters related to light. It was reported in previous studies that
 400 particulate nitrate photolysis is a source of HONO (Ye et al., 2017; Ye et al., 2016; Scharko et al., 2014; Romer et al., 2018;
 401 Mcfall et al., 2018). We will discuss the possibility of HONO being produced by photolysis of particulate nitrate ($J(\text{NO}_3\text{-R})$
 402 $\times \text{pNO}_3^-$) at this site in this section. There was a logarithmic relationship showing good correlation between R_{unknown} ($\text{ppb}\cdot\text{h}^{-1}$)
 403 and $J(\text{NO}_3\text{-R}) \times \text{pNO}_3^-$ ($\mu\text{g}\cdot\text{m}^{-3}\cdot\text{s}^{-1}$) in spring ($R^2 = 0.6519$) and summer ($R^2 = 0.6511$), while relatively weak correlation was
 404 found in autumn ($R^2 = 0.3633$) and winter ($R^2 = 0.4186$) (Fig. 9). This result indicated that photolysis of particulate nitrate
 405 contributed more in spring and summer than in autumn and winter. In conditions of relatively lower $J(\text{NO}_3\text{-R}) \times \text{pNO}_3^-$,
 406 R_{unknown} increased rapidly with increasing pNO_3^- concentration and its photolysis rate constant but reached a plateau after a
 407 critical value ($J(\text{NO}_3\text{-R}) \times \text{pNO}_3^- > 0.5 \mu\text{g}\cdot\text{m}^{-3}\cdot\text{s}^{-1}$ in summer, $J(\text{NO}_3\text{-R}) \times \text{pNO}_3^- > 0.4 \mu\text{g}\cdot\text{m}^{-3}\cdot\text{s}^{-1}$ in autumn, and $J(\text{NO}_3\text{-R})$
 408 $\times \text{pNO}_3^- > 1.5 \mu\text{g}\cdot\text{m}^{-3}\cdot\text{s}^{-1}$ in winter). There was no obvious turning point in spring, but it could be seen that the growth rate
 409 was declining. This indicated that in conditions that were relatively cleaner, the missing daytime source of HONO was limited
 410 by the pNO_3^- concentration and the photolysis rate constant. However, with enough particulate nitrate providing sufficient
 411 precursor or enough light to stimulate the reaction, the HONO production did not increase as $J(\text{NO}_3\text{-R}) \times \text{pNO}_3^-$ increased.
 412 Other generation mechanisms might play leading roles in the condition with enough particulate nitrate or enough light. It was
 413 found in a previous study that heterogeneous soot photochemistry may contribute to the daytime HONO concentration (Monge
 414 et al., 2010). Black carbon (BC) values were as a substitute for soot values (Sörgel et al., 2011). When BC concentration was
 415 above $2.0 \mu\text{g}\cdot\text{m}^{-3}$, the missing daytime source of HONO did not increase as $J(\text{NO}_3\text{-R}) \times \text{pNO}_3^-$ increased. We found that the
 416 missing daytime source of HONO correlated better with $\text{BC}\times\text{UV}$ ($R=0.9269$, $R=0.6356$) than with BC ($R=0.4776$, $R=0.6071$)
 417 or UV ($R=0.8494$, $R=0.4262$) alone in autumn and winter (Fig. S4), probably related to the conversion of NO_2 to HONO on
 418 BC enhanced by light.

419 We discuss whether photolysis of particulate nitrate was able to provide enough additional HONO by estimating the rate of
 420 HONO production by nitrate photolysis in spring and summer (Zhou et al., 2007; Li et al., 2012; Wang et al., 2017) using

$$421 J_{\text{NO}_3^- \rightarrow \text{HONO}} = \frac{R_{\text{unknown}} \times H}{f \times [\text{NO}_3^-] \times v_{\text{NO}_3^-} \times t_d}, \quad (7)$$

422 where $J_{\text{NO}_3^- \rightarrow \text{HONO}}$ is the rate of photolysis of NO_3^- to form HONO, $v_{\text{NO}_3^-}$ is the dry deposition rate of NO_3^- during the period
 423 t_d , and f is the proportion of the surface exposed to the sun at midday. Here, we suppose that the surfaces involving NO_3^- were
 424 exposed to light by a factor $f = 1/4$, taking mixing height $H = 200 \text{ m}$, $v_{\text{NO}_3^-} = 5 \text{ cm}\cdot\text{s}^{-1}$ over $t_d = 24 \text{ h}$. We use the mean
 425 midday value of $R_{\text{unknown}} = 9.72 \mu\text{g}\cdot\text{m}^{-3}\cdot\text{h}^{-1}$ and $[\text{NO}_3^-] = 10.35 \mu\text{g}\cdot\text{m}^{-3}$ in spring; and $R_{\text{unknown}} = 11.51 \mu\text{g}\cdot\text{m}^{-3}\cdot\text{h}^{-1}$ and
 426 $[\text{NO}_3^-] = 2.86 \mu\text{g}\cdot\text{m}^{-3}$ in summer. The photolysis rates $J_{\text{NO}_3^- \rightarrow \text{HONO}}$ derived from Eq. (8) were $4.83 \times 10^{-5} \text{ s}^{-1}$ and
 427 $2.07 \times 10^{-4} \text{ s}^{-1}$ for spring and summer, respectively. These values were in the range 6.2×10^{-6} to 5.0×10^{-4} obtained in a

428 previous study (Ye et al., 2017), which indicated that particulate nitrate photolysis could be likely source for the missing
429 daytime additional HONO formation in spring and summer. The variability of $J_{\text{NO}_3^- \rightarrow \text{HONO}}$ may be caused by chemical
430 composition, acidity, light-absorbing constituents, and the optical and other physical properties of aerosols.

431 3.5 Parameterization of HONO

432 Through an empirical parameterized formula, we can explore an accurate parameterization method for HONO, discuss the
433 main control factors for the HONO concentration and its chemical behavior, and quantify its main sources and key kinetic
434 parameters. As mentioned in Sect. 3.1, the HONO/NO_x ratio is better than HONO/NO₂ as an indicator of HONO generation.
435 In another study (Elshorbany et al., 2012), data were collected from 15 field observations all over the world to establish the
436 correlation between the HONO/NO_x ratio and the HONO concentration in global models. Therefore, we applied this method
437 in this study to parameterize the HONO concentration. As shown in Fig. 10, the $\Delta\text{HONO}/\Delta\text{NO}_x$ ratios in the four seasons were
438 close to the calculated value (0.02). However, there were seasonal variations in the slope, showing a maximum in summer
439 (2.60×10^{-2}), followed by autumn (2.06×10^{-2}), and a minimum in winter (1.59×10^{-2}). Except for in spring, HONO showed
440 good correlation with NO_x, with R^2 values ranging from 0.8972 to 0.9621. Therefore, we used slopes of 2.60×10^{-2} , 2.06×10^{-2} ,
441 and 1.59×10^{-2} to parameterize the HONO concentrations in summer, autumn, and winter, respectively. As for spring, though
442 only a weak correlation between HONO and NO_x was found, the majority of the $\Delta\text{HONO}/\Delta\text{NO}_x$ ratios fluctuated round a slope
443 of 0.02 because concentrations of NO_x greater than 60 ppb only accounted for 8.83 % of the data. Therefore, a slope of 0.02
444 was applied in spring to parameterize the HONO concentration.

445 As can be seen from Fig. 11, the estimated values are very close to the observed values in the nighttime in autumn. After
446 sunrise and before noon, the values observed were higher than the estimated values, and this difference gradually increases.
447 After noon and before sunset, the values observed were still higher than the values estimated, but the difference gradually
448 decreases. This phenomenon was also found in the daytime in spring and summer, but not in winter. Compared with the
449 daytime, the estimated values during the nighttime were closer to the observed values in both trend and value in all four seasons,
450 which further demonstrates that nighttime HONO is mainly produced from the direct vehicle emissions and heterogeneous
451 reaction of NO₂ on the ground or the surfaces of aerosols. Therefore, we should pay much more attention to simulation in the
452 daytime. We distinguish two main sectors, nighttime and daytime, to analyze the factors affecting the HONO diurnal variation
453 (Liu, 2017). Although $J(\text{HONO}) \times \text{HONO}$ also correlated well with $J(\text{NO}_2) \times \text{NO}_2$ in all four seasons in this study and the linear
454 fitting coefficients fluctuated around 0.01 in all four seasons (Fig. S5), bad simulation results during the daytime were found
455 (Fig. S6) using

$$456 [\text{HONO}] = k \times [\text{NO}_2] \times J(\text{NO}_2) / J(\text{HONO}). \quad (8)$$

457 Where k was the linear fitting coefficient between $J(\text{HONO}) \times \text{HONO}$ and $J(\text{NO}_2) \times \text{NO}_2$. In contrast, excellent simulation results
458 were found in a previous study using the same formula (Liu, 2017), which suggests that using the same simulation formula in

459 different regions may obtain greatly varying results. Eq. (8) can be regarded as a combination of $[\text{NO}_2]$ with $J(\text{NO}_2)/J(\text{HONO})$.
 460 $J(\text{NO}_2)/J(\text{HONO})$ kept relatively constant (5.48~5.87) in the daytime in four seasons. Therefore, diurnal variation of $[\text{HONO}]$
 461 simulated by Eq. (8) depended on $[\text{NO}_2]$ (Fig. S7). Eq. (8) is only suitable for regions where the diurnal variation of $[\text{NO}_2]$ is
 462 consistent with that of $[\text{HONO}]$.

463 As discussed in Sect. 3.4.2, nitrate photolysis was perhaps the source of HONO in this study. Besides, the difference between
 464 the observed value and the simulated value kept increasing before noon and the difference began to decrease after noon, which
 465 was consistent with nitrate photolysis. Therefore, we take the photolysis of nitrate into the HONO concentration simulation.
 466 The specific formulas for the simulation of spring, summer, autumn and winter as shown as follow:

$$467 \text{ HONO}_{\text{spring}} = 2.00 \times 10^{-2} \times \text{NO}_x + [\text{NO}_3^-] \times J(\text{NO}_{3-R})/4 \quad (9)$$

$$468 \text{ HONO}_{\text{summer}} = 2.60 \times 10^{-2} \times \text{NO}_x + [\text{NO}_3^-] \times J(\text{NO}_{3-R}) \quad (10)$$

$$469 \text{ HONO}_{\text{autumn}} = 2.06 \times 10^{-2} \times \text{NO}_x + [\text{NO}_3^-] \times J(\text{NO}_{3-R}) \quad (11)$$

$$470 \text{ HONO}_{\text{winter}} = 1.59 \times 10^{-2} \times \text{NO}_x + [\text{NO}_3^-] \times J(\text{NO}_{3-R})/4 \quad (12)$$

471 In this way, the daytime simulation results are significantly improved (Fig. 11). This further demonstrates that the
 472 apportionment of HONO sources is credible. The parameterization described in this work was more reasonable and can be
 473 better used in the future in such coastal sites.

474 3.6 Comparison of contributions of HONO and O₃ to OH radicals

475 Comparing the OH radical production via photolysis of HONO and O₃, the effect of the high HONO concentrations in the
 476 daytime on the tropospheric oxidation capacity was evaluated (Ryan et al., 2018). Nitrous acid is considered to be a crucial
 477 source of OH radicals (Lee et al., 2016). As shown in Eq. (12), OH production rates from O₃ photolysis ($P_{\text{OH}}(\text{O}_3)$) were
 478 calculated based on $[\text{O}_3]$, $J(\text{O}^1\text{D})$, and $[\text{H}_2\text{O}]$ (Liu et al., 2019a). Only O(¹D) atoms produced by the O₃ photolysis at UV
 479 wavelengths less than 320 nm (R6) can combine with water to generate OH radicals (R7) in the atmosphere. The absolute
 480 water concentration was derived from temperature and RH. The reaction (R8) rates for N₂ is $3.1 \times 10^{-11} \text{ cm}^3 \text{ molecules}^{-1} \text{ s}^{-1}$
 481 and for O₂ is $4.0 \times 10^{-11} \text{ cm}^3 \text{ molecules}^{-1} \text{ s}^{-1}$ (Liu et al., 2019a). The net OH formation from HONO was estimated by Eq. (13)
 482 (Su et al., 2008a; Sörgel et al., 2011; Li et al., 2018a; Atkinson et al., 2004). In addition to the two primary production of OH
 483 radicals mentioned above, there are the reaction of organic and hydro peroxy radicals (RO₂ and HO₂) with NO, hydrogen
 484 peroxide photolysis and the ozonolysis of alkenes (Hofzumahaus et al., 2009; Gligorovski et al., 2015; Wang et al., 2018).

$$485 P_{\text{OH}}(\text{O}_3) = 2J(\text{O}^1\text{D})[\text{O}_3]\phi\text{OH}, \quad \phi\text{OH} = k_7[\text{H}_2\text{O}]/(k_7[\text{H}_2\text{O}] + k_8[M]) \quad (12)$$





489 $P_{OH}(HONO) = J_{HONO}[HONO] - k_{OH+NO}[NO][OH] - k_{OH+HONO}[HONO][OH]$ (13)

490 The diurnal patterns of $P(OH)$ are shown in Fig. 12. The formation rates of OH from O_3 photolysis peaked in midday at around
491 $0.71 \text{ ppb}\cdot\text{h}^{-1}$, $5.80 \text{ ppb}\cdot\text{h}^{-1}$, $2.21 \text{ ppb}\cdot\text{h}^{-1}$, and $0.48 \text{ ppb}\cdot\text{h}^{-1}$ for spring, summer, autumn, and winter, respectively. The variation
492 of $P_{OH}(O_3)$ is consistent with $J(O^1D)$ (Fig. S8), peaking in midday and in summer on a diurnal and a seasonal timescale,
493 respectively. For summer and autumn, $P_{OH}(HONO)$ had a similar trend as $P_{OH}(O_3)$, peaking at around noon at the time of the
494 highest $J(HONO)$, but this was negligible at sunrise and sunset (Fig. S9). For spring and winter, however, $P_{OH}(HONO)$ reached
495 a maximum in the morning rush hour caused by the combined influences of high HONO concentration and high $J(HONO)$. A
496 similar result was also found in southwest Spain from mid-November to mid-December 2008 (Sörgel et al., 2011). The HONO
497 photolysis contributed significantly more OH than O_3 photolysis during the whole daytime in spring, autumn, and winter. In
498 summer, the HONO photolysis contributed to more OH in the early morning, and although the O_3 photolysis produced more
499 in the afternoon, HONO photolysis had a considerable effect on OH production. A similar result was also found in Nanjing of
500 eastern China from November 2017 to November 2018 (Liu et al., 2019a). These results show that HONO contributes
501 considerably to the atmospheric oxidizing capacity of the suburban atmosphere of Xiamen. Although HONO concentrations
502 (average: 0.66 ppb) are much lower than O_3 concentrations (average: 35.88 ppb) during 07:00–16:00 LT, daytime HONO
503 photolysis forms significantly more OH than daytime photolysis of O_3 in four seasons except for summer afternoon. Generally,
504 the mean value of $P_{OH}(HONO)$ from 07:00 to 16:00 LT was $1.89 \text{ ppb}\cdot\text{h}^{-1}$, and the average $P_{OH}(O_3)$ was $1.14 \text{ ppb}\cdot\text{h}^{-1}$. A similar
505 result was found in Melbourne, where the peak OH production rate reached $2 \text{ ppb}\cdot\text{h}^{-1}$ from 0.4 ppb HONO (Ryan et al., 2018).
506 The important role of HONO in the production of OH promotes photochemical peroxyacetyl nitrate formation (Hu et al., 2020).

507 4. Conclusions

508 We conducted measurements of HONO in the atmosphere at an IUE supersite in a coastal city of southeastern China in August,
509 October, and December 2018 and March 2019, finding an average HONO concentration of $0.54 \pm 0.47 \text{ ppb}$ across the whole
510 observation period. Concentrations of HONO in spring and summer were higher than in winter and autumn, which was
511 consistent with seasonal variations in RH. Both higher HONO concentrations in the daytime and the HONO/ NO_x ratio peaking
512 around noon suggested that additional sources of HONO might be related to light. It was found that the contribution from
513 vehicle exhaust emissions (1.45%) was higher than that found in most other studies due to the site being surrounded by several
514 expressways with a large number of passing diesel vehicles. The average nocturnal conversion rate of NO_2 to HONO was
515 0.46% h^{-1} , which was within the range 0.29 – 2.40% h^{-1} found by other studies. The HONO_{corr}/ NO_2 ratio increased with RH
516 and the concentration of $PM_{2.5}$ during the nighttime, which indicates that nocturnal heterogeneous reactions on the surfaces of
517 aerosols are the major source of HONO. However, dark heterogeneous formation (P_{hete}) was almost negligible in the daytime,
518 accounting for approximately 8.31% of known sources across the whole observation period. $R_{unknown}$ made up at the largest

519 proportion of all sources in summer (81.25 %), autumn (73.99 %), spring (70.87 %), and winter (59.28 %). It was found that
520 there was a logarithmic relationship between R_{unknown} and particulate nitrate photolysis in four seasons. The variation of HONO
521 at night can be accurately simulated based on the HONO/NO_x ratio, while $J(\text{NO}_3^- \text{-R}) \times \text{pNO}_3^-$ or $1/4 \times (J(\text{NO}_3^- \text{-R}) \times \text{pNO}_3^-)$
522 should be considered for daytime simulation. Local tropospheric oxidation capacity was significantly increased by HONO
523 during 07:00–16:00, providing an OH radical source 1.89 ppb·h⁻¹.

524 **Data availability**

525 The observation data at this site are available from the authors upon request.

526 **Authorship Contribution Statement**

527 Baoye Hu and Jun Duan contributed equally to this work. Baoye Hu and Jun Duan collected the HONO data and analyzed the
528 data. Baoye Hu wrote the manuscript. Baoye Hu, Jun Duan performed the experiments. Jun Duan and Fang Wu built equipment
529 of IBBCEEAS. Youwei Hong, Min Qin and Jinsheng Chen revised manuscript. Min Qin, Pinhua Xie and Jinsheng Chen
530 designed the manuscript. Jinsheng Chen supported funding of observation and research. Lingling Xu, Mengren Li, Yahui Bian
531 contributed to discussions of results.

532 **Competing interests**

533 The authors declare that they have no conflict of interest.

534 **Acknowledgments**

535 This study was funded by the Cultivating Project of Strategic Priority Research Program of Chinese Academy of Sciences
536 (XDPB1903), the National Key Research and Development Program (2017YFC0209400, 2016YFC02005,
537 2016YFC0112200), the National Natural Science Foundation of China (41575146, 41875154), the FJIRSM&IUE Joint
538 Research Fund (RHZX-2019-006), the Center for Excellence in Regional Atmospheric Environment, CAS (E0L1B20201),
539 State Key Laboratory of Environmental Chemistry and Ecotoxicology, Research Center for Eco-Environmental Sciences, CAS
540 and Xiamen Atmospheric Environment Observation and Research Station of Fujian Province.

541 **Supplementary information**

542 Attached please find supplementary information associated with this article.

543 References

- 544 Acker, K., Febo, A., Trick, S., Perrino, C., Bruno, P., Wiesen, P., Möller, D., Wieprecht, W., Auel, R., Giusto, M., Geyer, A., Platt, U., and
545 Allegrini, I.: Nitrous acid in the urban area of Rome, *Atmos. Environ.*, 40, 3123-3133, 10.1016/j.atmosenv.2006.01.028, 2006.
- 546 Aliche, B.: Impact of nitrous acid photolysis on the total hydroxyl radical budget during the Limitation of Oxidant Production/Pianura Padana
547 Produzione di Ozono study in Milan, *J. Geophys. Res.*, 107, 10.1029/2000jd000075, 2002.
- 548 Ammann, M., Kalberer, M., Jost, D. T., Tobler, L., Roßler, E., Piguet, D., Gaggeler, H. W., and Baltensperger, U.: Heterogeneous
549 production of nitrous acid on soot in polluted air masses, *Nature*, 395, 157-160, 1998.
- 550 Atkinson, R., Baulch, D. L., Cox, R. A., Crowley, J. N., Hampson, R. F., Hynes, R. G., Jenkin, M. E., Rossi, M. J., and Troe, J.: Evaluated
551 kinetic and photochemical data for atmospheric chemistry: Volume I – gas phase reactions of Ox, HOx, NOx and SOx species, *Atmos. Chem.*
552 *Phys.*, 4, 1461–1738, 2004.
- 553 Aubin, D. G. and Abbatt, J. P.: Interaction of NO₂ with hydrocarbon soot: Focus on HONO yield, surface modification, and mechanism, *J.*
554 *Phys. Chem. A* 111, 6263-6273, 2007.
- 555 Chang, Y., Zou, Z., Deng, C., Huang, K., Collett, J. L., Lin, J., and Zhuang, G.: The importance of vehicle emissions as a source of
556 atmospheric ammonia in the megacity of Shanghai, *Atmos. Chem. Phys.*, 16, 3577-3594, 10.5194/acp-16-3577-2016, 2016.
- 557 Cui, L., Li, R., Zhang, Y., Meng, Y., Fu, H., and Chen, J.: An observational study of nitrous acid (HONO) in Shanghai, China: The aerosol
558 impact on HONO formation during the haze episodes, *Sci. Total. Environ.*, 630, 1057-1070, 10.1016/j.scitotenv.2018.02.063, 2018.
- 559 Duan, J., Qin, M., Ouyang, B., Fang, W., Li, X., Lu, K., Tang, K., Liang, S., Meng, F., Hu, Z., Xie, P., Liu, W., and Häsler, R.: Development
560 of an incoherent broadband cavity-enhanced absorption spectrometer for in situ measurements of HONO and NO₂, *Atmos. Meas. Tech.*, 11,
561 4531–4543, 10.5194/amt-11-4531-2018, 2018.
- 562 Elshorbany, Y. F., Steil, B., Brühl, C., and Lelieveld, J.: Impact of HONO on global atmospheric chemistry calculated with an empirical
563 parameterization in the EMAC model, *Atmos. Chem. Phys.*, 12, 9977-10000, 10.5194/acp-12-9977-2012, 2012.
- 564 Elshorbany, Y. F., Kurtenbach, R., Wiesen, P., Lissi, E., Rubio, M., Villena, G., Gramsch, E., Rickard, A. R., Pilling, M. J., and Kleffmann,
565 J.: Oxidation capacity of the city air of Santiago, Chile, *Atmos. Chem. Phys.*, 9, 2257–2273, <https://www.atmos-chem-phys.net/9/2257/2009/>,
566 2009.
- 567 Finlayson-Pitts, B. J., Wingen, L. M., Sumner, A. L., Syomin, D., and Ramazan, K. A.: The heterogeneous hydrolysis of NO₂ in laboratory
568 systems and in outdoor and indoor atmospheres: An integrated mechanism, *Phys. Chem. Chem. Phys.*, 5, 223-242, 10.1039/b208564j, 2003.
- 569 Fu, X., Wang, T., Zhang, L., Li, Q., Wang, Z., Xia, M., Yun, H., Wang, W., Yu, C., Yue, D., Zhou, Y., Zheng, J., and Han, R.: The significant
570 contribution of HONO to secondary pollutants during a severe winter pollution event in southern China, *Atmos. Chem. Phys.*, 19, 1-14,
571 10.5194/acp-19-1-2019, 2019.
- 572 Gao, J.: An analysis of some pollution weather conditions, *Journal of Oceanography in Taiwan Strait*, 18, 55-62, 1999.
- 573 Ge, S., Wang, G., Zhang, S., Li, D., Xie, Y., Wu, C., Yuan, Q., Chen, J., and Zhang, H.: Abundant NH₃ in China Enhances Atmospheric
574 HONO Production by Promoting the Heterogeneous Reaction of SO₂ with NO₂, *Environ. Sci. Technol.*, 53, 14339-14347,
575 10.1021/acs.est.9b04196, 2019.
- 576 George, C., Strekowski, R. S., Kleffmann, J., Stemmler, K., and Ammann, M.: Photoenhanced uptake of gaseous NO₂ on solid organic
577 compounds: a photochemical source of HONO?, *Faraday Discuss*, 130, 195-210; discussion 241-164, 519-124, 10.1039/b417888m, 2005.
- 578 Gil, J., Kim, J., Lee, M., Lee, G., Lee, D., Jung, J., An, J., Hong, J., Cho, S., Lee, J., and Long, R.: The role of HONO in O₃ formation and
579 insight into its formation mechanism during the KORUS-AQ Campaign, *Atmos. Chem. Phys. Discuss*, 10.5194/acp-2019-1012, 2019.
- 580 Gligorovski, S., Strekowski, R., Barbati, S., and Vione, D.: Environmental Implications of Hydroxyl Radicals (*OH), *Chem. Rev.*, 115,
581 13051-13092, 10.1021/cr500310b, 2015.
- 582 Gutzwiller, L., Arens, F., Baltensperger, U., Gaggeler, H. W., and Ammann, M.: Significance of Semivolatile Diesel Exhaust Organics for
583 Secondary HONO Formation, *Environ. Sci. Technol.*, 36, 677-682, 2002.

- 584 He, Y., Zhou, X., Hou, J., Gao, H., and Bertman, S. B.: Importance of dew in controlling the air-surface exchange of HONO in rural forested
585 environments, *Geophys. Res. Lett.*, 33, 10.1029/2005gl024348, 2006.
- 586 Hofzumahaus, A., Rohrer, F., Lu, K., Bohn, B., Brauers, T., Chang, C.-C., Fuchs, H., Holland, F., Kita, K., Kondo, Y., Li, X., Lou, S., Shao,
587 M., Zeng, L., Wahner, A., and Zhang, Y.: Amplified Trace Gas Removal in the Troposphere, *Science*, 324, 1702-1704, 2009.
- 588 Hou, S., Tong, S., Ge, M., and An, J.: Comparison of atmospheric nitrous acid during severe haze and clean periods in Beijing, China, *Atmos.*
589 *Environ.*, 124, 199-206, 10.1016/j.atmosenv.2015.06.023, 2016.
- 590 Hu, B., Liu, T., Hong, Y., Xu, L., Li, M., Wu, X., Wang, H., Chen, J., and Chen, J.: Characteristics of peroxyacetyl nitrate (PAN) in a coastal
591 city of southeastern China: Photochemical mechanism and pollution process, *Sci. Total Environ.*, 719, 137493,
592 10.1016/j.scitotenv.2020.137493, 2020.
- 593 Huang, R. J., Yang, L., Cao, J., Wang, Q., Tie, X., Ho, K. F., Shen, Z., Zhang, R., Li, G., Zhu, C., Zhang, N., Dai, W., Zhou, J., Liu, S.,
594 Chen, Y., Chen, J., and O'Dowd, C. D.: Concentration and sources of atmospheric nitrous acid (HONO) at an urban site in Western China,
595 *Sci. Total Environ.*, 593-594, 165-172, 10.1016/j.scitotenv.2017.02.166, 2017.
- 596 Jenkin, M. E., Cox, R. A., and Williams, D. J.: Laboratory studies of the kinetics of formation of nitrous acid from the thermal reaction of
597 nitrogen dioxide and water vapour, *Atmos. Environ.*, 22, 487-498, 1988.
- 598 Kasibhatla, P., Sherwen, T., Evans, M. J., Carpenter, L. J., Reed, C., Alexander, B., Chen, Q., Sulprizio, M. P., Lee, J. D., Read, K. A., Bloss,
599 W., Crilley, L. R., Keene, W. C., Pszenny, A. A. P., and Hodzic, A.: Global impact of nitrate photolysis in sea-salt aerosol on NO_x, OH, and
600 O₃ in the marine boundary layer, *Atmos. Chem. Phys.*, 18, 11185-11203, 10.5194/acp-18-11185-2018, 2018.
- 601 Kirchner, U., Scheer, V., and Vogt, R.: FTIR Spectroscopic Investigation of the Mechanism and Kinetics of the Heterogeneous Reactions
602 of NO₂ and HNO₃ with Soot, *J. Phys. Chem. A*, 104, 8908-8915, 2000.
- 603 Kirchstetter, T. W., Harley, R. A., and Littlejohn, D.: Measurement of Nitrous Acid in Motor Vehicle Exhaust, *Environ. Sci. Technol.*, 30,
604 2843-2849, 1996.
- 605 Kleffmann, J.: Daytime formation of nitrous acid: A major source of OH radicals in a forest, *Geophys. Res. Lett.*, 32, 10.1029/2005gl022524,
606 2005.
- 607 Kleffmann, J.: Daytime sources of nitrous acid (HONO) in the atmospheric boundary layer, *Chem. phys. chem*, 8, 1137-1144,
608 10.1002/cphc.200700016, 2007.
- 609 Kleffmann, J., Becker, K., and Wiesen, P.: Heterogeneous NO₂ conversion processes on acid surfaces: Possible atmospheric implications,
610 *Atmos. Environ.*, 32, 2721-2729, [https://doi.org/10.1016/S1352-2310\(98\)00065-X](https://doi.org/10.1016/S1352-2310(98)00065-X), 1998.
- 611 Kramer, L. J., Crilley, L. R., Adams, T. J., Ball, S. M., Pope, F. D., and Bloss, W. J.: Nitrous acid (HONO) emissions under real-world
612 driving conditions from vehicles in a UK road tunnel, *Atmos. Chem. Phys.*, 20, 5231-5248, 10.5194/acp-20-5231-2020, 2020.
- 613 Kurtenbacha, R., Beckera, K. H., Gomesa, J. A. G., Kleffmann, J., Lorzera, J. C., Spittler, M., Wiesena, P., Ackermannb, R., Geyerb, A.,
614 and Plattb, U.: Investigations of emissions and heterogeneous formation of HONO in a road traffic tunnel, *Atmos. Environ.*, 35, 3385-3394,
615 2001.
- 616 Lee, B. H., Wood, E. C., Herndon, S. C., Lefer, B. L., Luke, W. T., Brune, W. H., Nelson, D. D., Zahniser, M. S., and Munger, J. W.: Urban
617 measurements of atmospheric nitrous acid: A caveat on the interpretation of the HONO photostationary state, *J. Geophys. Res. Atmos.*, 118,
618 12,274-212,281, 10.1002/2013jd020341, 2013.
- 619 Lee, J. D., Whalley, L. K., Heard, D. E., Stone, D., Dunmore, R. E., Hamilton, J. F., Young, D. E., Allan, J. D., Laufs, S., and Kleffmann,
620 J.: Detailed budget analysis of HONO in central London reveals a missing daytime source, *Atmos. Chem. Phys.*, 16, 2747-2764, 10.5194/acp-
621 16-2747-2016, 2016.
- 622 Lei, L., Zhiyao, D., Hui Li, Chongqin Zhu, Graeme Henkelman, Joseph S. Francisco, and Zeng, X. C.: Formation of HONO from the NH₃-
623 promoted hydrolysis of NO₂ dimers in the atmosphere, *Proc. Natl. Acad. Sci. USA*, 115, 7236-7241,
624 <https://doi.org/10.1073/pnas.1807719115> 2018.
- 625 Li, D., Xue, L., Wen, L., Wang, X., Chen, T., Mellouki, A., Chen, J., and Wang, W.: Characteristics and sources of nitrous acid in an urban
626 atmosphere of northern China: Results from 1-yr continuous observations, *Atmos. Environ.*, 182, 296-306, 10.1016/j.atmosenv.2018.03.033,
627 2018a.
- 628 Li, G., Lei, W., Zavala, M., Volkamer, R., Dusanter, S., Stevens, P., and Molina, L. T.: Impacts of HONO sources on the photochemistry in
629 Mexico City during the MCMA-2006/MILAGO Campaign, *Atmos. Chem. Phys.*, 10, 6551-6567, 10.5194/acp-10-6551-2010, 2010.

- 630 Li, L., Duan, Z., Li, H., Zhu, C., Henkelman, G., Francisco, J. S., and Zeng, X. C.: Formation of HONO from the NH₃-promoted hydrolysis
631 of NO₂ dimers in the atmosphere, *Proc. Natl. Acad. Sci. U S A*, 115, 7236-7241, 10.1073/pnas.1807719115, 2018b.
- 632 Li, S., Matthews, J., and Sinha, A.: Atmospheric Hydroxyl Radical Production from Electronically Excited NO₂ and H₂O, *Science*, 319,
633 2008.
- 634 Li, X., Brauers, T., Häsel, R., Bohn, B., Fuchs, H., Hofzumahaus, A., Holland, F., Lou, S., Lu, K. D., Rohrer, F., Hu, M., Zeng, L. M.,
635 Zhang, Y. H., Garland, R. M., Su, H., Nowak, A., Wiedensohler, A., Takegawa, N., Shao, M., and Wahner, A.: Exploring the atmospheric
636 chemistry of nitrous acid (HONO) at a rural site in Southern China, *Atmos. Chem. Phys.*, 12, 1497-1513, 10.5194/acp-12-1497-2012, 2012.
- 637 Li, X., Rohrer, F., Hofzumahaus, A., Brauers, T., Häsel, R., Bohn, B., Broch, S., Fuchs, H., Gomm, S., Holland, F., Jäger, J., Kaiser, J.,
638 Keutsch, F. N., Lohse, I., Lu, K., Tillmann, R., Wegener, R., Wolfe, G. M., Mentel, T. F., Kiendler-Scharr, A., and Wahner, A.: Missing
639 Gas-Phase Source of HONO Inferred from Zeppelin Measurements in the Troposphere, *Science*, 344, 2014.
- 640 Liu, Y.: Observations and parameterized modelling of ambient nitrous acid (HONO) in the megacity areas of the eastern China Peking
641 University, China, 161 pp., 2017.
- 642 Liu, Y., Nie, W., Xu, Z., Wang, T., Wang, R., Li, Y., Wang, L., Chi, X., and Ding, A.: Semi-quantitative understanding of source contribution
643 to nitrous acid (HONO) based on 1 year of continuous observation at the SORPES station in eastern China, *Atmos. Chem. Phys.*, 19, 13289-
644 13308, 10.5194/acp-19-13289-2019, 2019a.
- 645 Liu, Y., Lu, K., Li, X., Dong, H., Tan, Z., Wang, H., Zou, Q., Wu, Y., Zeng, L., Hu, M., Min, K. E., Kecorius, S., Wiedensohler, A., and
646 Zhang, Y.: A Comprehensive Model Test of the HONO Sources Constrained to Field Measurements at Rural North China Plain, *Environ.*
647 *Sci. Technol.*, 10.1021/acs.est.8b06367, 2019b.
- 648 Liu, Z., Wang, Y., Costabile, F., Amoroso, A., Zhao, C., Huey, L. G., Stickel, R., Liao, J., and Zhu, T.: Evidence of aerosols as a media for
649 rapid daytime HONO production over China, *Environ Sci Technol*, 48, 14386-14391, 10.1021/es504163z, 2014.
- 650 Lu, K. D., Hofzumahaus, A., Holland, F., Bohn, B., Brauers, T., Fuchs, H., Hu, M., Häsel, R., Kita, K., Kondo, Y., Li, X., Lou, S. R.,
651 Oebel, A., Shao, M., Zeng, L. M., Wahner, A., Zhu, T., Zhang, Y. H., and Rohrer, F.: Missing OH source in a suburban environment near
652 Beijing: observed and modelled OH and HO₂ concentrations in summer 2006, *Atmos. Chem. Phys.*, 13, 1057-1080, 10.5194/acp-13-1057-
653 2013, 2013.
- 654 Makkonen, U., Virkkula, A., M'antykentt'a, J., Hakola, H., Keronen, P., Vakkari, V., and Aalto, P. P.: Semi-continuous gas and inorganic
655 aerosol measurements at a Finnish urban site: comparisons with filters, nitrogen in aerosol and gas phases, and aerosol acidity, *Atmos. Chem.*
656 *Phys.*, 12, 5617-5631, 10.5194/acp-12-5617-2012, 2012.
- 657 McFall, A. S., Edwards, K. C., and Anastasio, C.: Nitrate Photochemistry at the Air-Ice Interface and in Other Ice Reservoirs, *Environ. Sci.*
658 *Technol.*, 52, 5710-5717, 10.1021/acs.est.8b00095, 2018.
- 659 Meusel, H., Kuhn, U., Reiffs, A., Mallik, C., Harder, H., Martinez, M., Schuladen, J., Bohn, B., Parchatka, U., Crowley, J. N., Fischer, H.,
660 Tomsche, L., Novelli, A., Hoffmann, T., Janssen, R. H. H., Hartogensis, O., Pikridas, M., Vrekoussis, M., Bourtsoukidis, E., Weber, B.,
661 Lelieveld, J., Williams, J., Poschl, U., Cheng, Y. F., and Su, H.: Daytime formation of nitrous acid at a coastal remote site in Cyprus indicating
662 a common ground source of atmospheric HONO and NO, *Atmos. Chem. Phys.*, 16, 14475-14493, 10.5194/acp-16-14475-2016, 2016.
- 663 Michoud, V., Colomb, A., Borbon, A., Miet, K., Beekmann, M., Camredon, M., Aumont, B., Perrier, S., Zapf, P., Siour, G., Ait-Helal, W.,
664 Afif, C., Kukui, A., Furger, M., Dupont, J. C., Haeffelin, M., and Doussin, J. F.: Study of the unknown HONO daytime source at a European
665 suburban site during the MEGAPOLI summer and winter field campaigns, *Atmos. Chem. Phys.*, 14, 2805-2822, 10.5194/acp-14-2805-2014,
666 2014.
- 667 Min, K. E., Washenfelder, R. A., Dubé, W. P., Langford, A. O., Edwards, P. M., Zarzana, K. J., Stutz, J., Lu, K., Rohrer, F., Zhang, Y., and
668 Brown, S. S.: A broadband cavity enhanced absorption spectrometer for aircraft measurements of glyoxal, methylglyoxal, nitrous acid,
669 nitrogen dioxide, and water vapor, *Atmos. Meas. Tech.*, 9, 423-440, 10.5194/amt-9-423-2016, 2016.
- 670 Monge, M. E., D'Anna, B., Mazri, L., Giroir-Fendler, A., Ammann, M., Donaldson, D. J., and George, C.: Light changes the atmospheric
671 reactivity of soot, *Proc. Natl. Acad. Sci. U S A*, 107, 6605-6609, 10.1073/pnas.0908341107, 2010.
- 672 Ndour, M., D'Anna, B., George, C., Ka, O., Balkanski, Y., Kleffmann, J., Stemmler, K., and Ammann, M.: Photoenhanced uptake of NO₂
673 on mineral dust: Laboratory experiments and model simulations, *Geophys. Res. Lett.*, 35, 10.1029/2007g1032006, 2008.
- 674 Nie, W., Ding, A. J., Xie, Y. N., Xu, Z., Mao, H., Kerminen, V.-M., Zheng, L. F., Qi, X. M., Huang, X., Yang, X.-Q., Sun, J. N., Herrmann,
675 E., Petäjä, T., Kulmala, M., and Fu, C. B.: Influence of biomass burning plumes on HONO chemistry in eastern China, *Atmos. Chem. Phys.*,
676 15 1147-1159, 10.5194/acp-15-1147-2015, 2015.

677 Oswald, R., Behrendt, T., Ermel, M., Wu, D., Su, H., Cheng, Y., Breuninger, C., Moravek, A., Mougou, E., Delon, C., Loubet, B.,
678 Pommerening-Roser, A., Sorgel, M., Poschl, U., Hoffmann, T., Andreae, M. O., Meixner, F. X., and Trebs, I.: HONO emissions from soil
679 bacteria as a major source of atmospheric reactive nitrogen, *Science*, 341, 1233-1235, 10.1126/science.1242266, 2013.

680 Park, S. S., Hong, S. B., Jung, Y. G., and Lee, J. H.: Measurements of PM₁₀ aerosol and gas-phase nitrous acid during fall season in a semi-
681 urban atmosphere, *Atmos. Environ.*, 38, 293-304, 10.1016/j.atmosenv.2003.09.041, 2004.

682 Perner, D. and Platt, U.: Detection of nitrous acid in the atmosphere by differential optical absorption, *Geophys. Res. Lett.*, 6, 917-920,
683 doi:10.1029/GL006i012p00917, 1979.

684 Qin, M., Xie, P., Su, H., Gu, J., Peng, F., Li, S., Zeng, L., Liu, J., Liu, W., and Zhang, Y.: An observational study of the HONO-NO₂
685 coupling at an urban site in Guangzhou City, South China, *Atmos. Environ.*, 43, 5731-5742, 10.1016/j.atmosenv.2009.08.017, 2009.

686 Rappenglück, B., Lubertino, G., Alvarez, S., Golovko, J., Czader, B., and Ackermann, L.: Radical precursors and related species from traffic
687 as observed and modeled at an urban highway junction, *J. Air Waste Manage. Assoc.*, 63, 1270-1286, 10.1080/10962247.2013.822438, 2013.

688 Röckmann, T., Walter, S., Bohn, B., Wegener, R., Spahn, H., Brauers, T., Tillmann, R., Schlosser, E., Koppmann, R., and Rohrer, F.: Isotope
689 effect in the formation of H₂ from H₂CO studied at the atmospheric simulation chamber SAPHIR, *Atmos. Chem. Phys.*, 10, 5343-5357,
690 10.5194/acp-10-5343-2010, 2010.

691 Romer, P. S., Wooldridge, P. J., Crouse, J. D., Kim, M. J., Wennberg, P. O., Dibb, J. E., Scheuer, E., Blake, D. R., Meinardi, S., Brosius,
692 A. L., Thames, A. B., Miller, D. O., Brune, W. H., Hall, S. R., Ryerson, T. B., and Cohen, R. C.: Constraints on Aerosol Nitrate Photolysis
693 as a Potential Source of HONO and NO_x, *Environ. Sci. Technol.*, 10.1021/acs.est.8b03861, 2018.

694 Ryan, R. G., Rhodes, S., Tully, M., Wilson, S., Jones, N., Frieß, U., and Schofield, R.: Daytime HONO, NO₂ and aerosol distributions from
695 MAX-DOAS observations in Melbourne, *Atmos. Chem. Phys.*, 18, 13969-13985, 10.5194/acp-18-13969-2018, 2018.

696 Scharko, N. K., Berke, A. E., and Raff, J. D.: Release of Nitrous Acid and Nitrogen Dioxide from Nitrate Photolysis in Acidic Aqueous
697 Solutions, *Environ. Sci. Technol.*, 48, 11991-12001, 10.1021/es503088x, 2014.

698 Seinfeld, J. H. and Pandis, S. N.: *Atmospheric Chemistry and Physics. From Air Pollution to Climate Changes*, 1998.

699 Shi, X., Ge, Y., Zheng, J., Ma, Y., Ren, X., and Zhang, Y.: Budget of nitrous acid and its impacts on atmospheric oxidative capacity at an
700 urban site in the central Yangtze River Delta region of China, *Atmos. Environ.*, 238, 117725, 10.1016/j.atmosenv.2020.117725, 2020.

701 Slanina, J., ten Brink, H. M., Otjes, R. P., Even, A., Jongejan, P., Khlystov, A., WaijersIjpelaan, A., and Hu, M.: The continuous analysis of
702 nitrate and ammonium in aerosols by the steam jet aerosol collector (SJAC): extension and validation of the methodology, *Atmos. Environ.*,
703 35, 2319-2330, 2001.

704 Sörgel, M., Regelin, E., Bozem, H., Diesch, J. M., Drewnick, F., Fischer, H., Harder, H., Held, A., Hosaynali-Beygi, Z., Martinez, M., and
705 Zetzsch, C.: Quantification of the unknown HONO daytime source and its relation to NO₂, *Atmos. Chem. Phys.*, 11, 10433-10447,
706 10.5194/acp-11-10433-2011, 2011.

707 Spataro, F., Ianniello, A., Esposito, G., Allegrini, I., Zhu, T., and Hu, M.: Occurrence of atmospheric nitrous acid in the urban area of Beijing
708 (China), *Sci. Total Environ.*, 447, 210-224, 10.1016/j.scitotenv.2012.12.065, 2013.

709 Stemmler, K., Ammann, M., Donders, C., Kleffmann, J., and George, C.: Photosensitized reduction of nitrogen dioxide on humic acid as a
710 source of nitrous acid, *Nature*, 440, 195-198, 10.1038/nature04603, 2006.

711 Stutz, J., Alicke, B., Ackermann, R., Geyer, A., Wang, S., White, A. B., Williams, E. J., Spicer, C. W., and Fast, J. D.: Relative humidity
712 dependence of HONO chemistry in urban areas, *J. Geophys. Res. Atmos.*, 109, n/a-n/a, 10.1029/2003jd004135, 2004.

713 Su, H., Cheng, Y. F., Shao, M., Gao, D. F., Yu, Z. Y., Zeng, L. M., Slanina, J., Zhang, Y. H., and Wiedensohler, A.: Nitrous acid (HONO)
714 and its daytime sources at a rural site during the 2004 PRIDE-PRD experiment in China, *J. Geophys. Res.*, 113, 10.1029/2007jd009060,
715 2008a.

716 Su, H., Cheng, Y., Oswald, R., Behrendt, T., Trebs, I., Meixner, F. X., Andreae, M. O., Cheng, P., Zhang, Y., and Pöschl, U.: Soil nitrite as
717 a source of atmospheric HONO and OH radicals, *Science*, 333, 1616-1618, 2011.

718 Su, H., Cheng, Y. F., Cheng, P., Zhang, Y. H., Dong, S., Zeng, L. M., Wang, X., Slanina, J., Shao, M., and Wiedensohler, A.: Observation
719 of nighttime nitrous acid (HONO) formation at a non-urban site during PRIDE-PRD2004 in China, *Atmos. Environ.*, 42, 6219-6232,
720 10.1016/j.atmosenv.2008.04.006, 2008b.

- 721 Tan, Z., Fuchs, H., Lu, K., Hofzumahaus, A., Bohn, B., Broch, S., Dong, H., Gomm, S., Häseler, R., He, L., Holland, F., Li, X., Liu, Y., Lu,
722 S., Rohrer, F., Shao, M., Wang, B., Wang, M., Wu, Y., Zeng, L., Zhang, Y., Wahner, A., and Zhang, Y.: Radical chemistry at a rural site
723 (Wangdu) in the North China Plain: observation and model calculations of OH, HO₂ and RO₂ radicals, *Atmos. Chem. Phys.*, 17, 663-690,
724 10.5194/acp-17-663-2017, 2017.
- 725 Tang, K., Qin, M., Duan, J., Fang, W., Meng, F., Liang, S., Xie, P., Liu, J., Liu, W., Xue, C., and Mu, Y.: A dual dynamic chamber system
726 based on IBBCEAS for measuring fluxes of nitrous acid in agricultural fields in the North China Plain, *Atmos. Environ.*, 196, 10-19,
727 10.1016/j.atmosenv.2018.09.059, 2019.
- 728 Underwood, G. M., Song, C. H., Phadnis, M., Carmichael, G. R., and Grassian, V. H.: Heterogeneous reactions of NO₂ and HNO₃ on oxides
729 and mineral dust: A combined laboratory and modeling study, *J. Geophys. Res.: Atmos.*, 106, 18055-18066, 10.1029/2000jd900552, 2001.
- 730 VandenBoer, T. C., Young, C. J., Talukdar, R. K., Markovic, M. Z., Brown, S. S., Roberts, J. M., and Murphy, J. G.: Nocturnal loss and
731 daytime source of nitrous acid through reactive uptake and displacement, *Nat. Geosci.*, 8, 55-60, 10.1038/ngeo2298, 2014.
- 732 VandenBoer, T. C., Brown, S. S., Murphy, J. G., Keene, W. C., Young, C. J., Pszenny, A. A. P., Kim, S., Warneke, C., de Gouw, J. A.,
733 Maben, J. R., Wagner, N. L., Riedel, T. P., Thornton, J. A., Wolfe, D. E., Dubé, W. P., Öztürk, F., Brock, C. A., Grossberg, N., Lefer, B.,
734 Lerner, B., Middlebrook, A. M., and Roberts, J. M.: Understanding the role of the ground surface in HONO vertical structure: High resolution
735 vertical profiles during NACHTT-11, *J. Geophys. Res.: Atmos.*, 118, 10,155-110,171, 10.1002/jgrd.50721, 2013.
- 736 Villena, G., Bejan, I., Kurtenbach, R., Wiesen, P., and Kleffmann, J.: Interferences of commercial NO₂ instruments in the urban atmosphere
737 and in a smog chamber, *Atmos. Meas. Tech.*, 5, 149-159, 10.5194/amt-5-149-2012, 2012.
- 738 Wang, H., Lyu, X., Guo, H., Wang, Y., Zou, S., Ling, Z., Wang, X., Jiang, F., Zeren, Y., Pan, W., Huang, X., and Shen, J.: Ozone pollution
739 around a coastal region of South China Sea: interaction between marine and continental air, *Atmos. Chem. Phys.*, 18, 4277-4295,
740 10.5194/acp-18-4277-2018, 2018.
- 741 Wang, J., Zhang, X., Guo, J., Wang, Z., and Zhang, M.: Observation of nitrous acid (HONO) in Beijing, China: Seasonal variation, nocturnal
742 formation and daytime budget, *Sci. Total Environ.*, 587-588, 350-359, 10.1016/j.scitotenv.2017.02.159, 2017.
- 743 Wang, L., Wen, L., Xu, C., Chen, J., Wang, X., Yang, L., Wang, W., Yang, X., Sui, X., Yao, L., and Zhang, Q.: HONO and its potential
744 source particulate nitrite at an urban site in North China during the cold season, *Sci. Total Environ.*, 538, 93-101,
745 10.1016/j.scitotenv.2015.08.032, 2015.
- 746 Wang, S.: Atmospheric observations of enhanced NO₂-HONO conversion on mineral dust particles, *Geophys. Res. Lett.*, 30,
747 10.1029/2003gl017014, 2003.
- 748 Wang, S., Zhou, R., Zhao, H., Wang, Z., Chen, L., and Zhou, B.: Long-term observation of atmospheric nitrous acid (HONO) and its
749 implication to local NO₂ levels in Shanghai, China, *Atmos. Environ.*, 77, 718-724, 10.1016/j.atmosenv.2013.05.071, 2013.
- 750 Wen, L., Chen, T., Zheng, P., Wu, L., Wang, X., Mellouki, A., Xue, L., and Wang, W.: Nitrous acid in marine boundary layer over eastern
751 Bohai Sea, China: Characteristics, sources, and implications, *Sci. Total Environ.*, 10.1016/j.scitotenv.2019.03.225, 2019.
- 752 Wong, K. W., Oh, H. J., Lefer, B. L., Rappenglück, B., and Stutz, J.: Vertical profiles of nitrous acid in the nocturnal urban atmosphere of
753 Houston, TX, *Atmos. Chem. Phys.*, 11, 3595-3609, 10.5194/acp-11-3595-2011, 2011.
- 754 Wyers, G. P., Otjes, R. P., and Slanina, J.: A continuous-flow denuder for the measurement of ambient concentrations and surface-exchange
755 fluxes of ammonia, *Atmos. Environ.*, 27, 2085-2090, 1993.
- 756 Xia, D., Zhang, X., Chen, J., Tong, S., Xie, H. B., Wang, Z., Xu, T., Ge, M., and Allen, D. T.: Heterogeneous Formation of HONO Catalyzed
757 by CO₂, *Environ Sci Technol*, 10.1021/acs.est.1c02706, 2021.
- 758 Xu, W., Kuang, Y., Zhao, C., Tao, J., Zhao, G., Bian, Y., Yang, W., Yu, Y., Shen, C., Liang, L., Zhang, G., Lin, W., and Xu, X.: NH₃-
759 promoted hydrolysis of NO₂ induces explosive growth in HONO, *Atmos. Chem. Phys.*, 19, 10557-10570, 10.5194/acp-19-10557-2019, 2019.
- 760 Xu, Z., Wang, T., Wu, J., Xue, L., Chan, J., Zha, Q., Zhou, S., Louie, P. K. K., and Luk, C. W. Y.: Nitrous acid (HONO) in a polluted
761 subtropical atmosphere: Seasonal variability, direct vehicle emissions and heterogeneous production at ground surface, *Atmos. Environ.*,
762 10.1016/j.atmosenv.2015.01.061, 2015.
- 763 Xun, A., Huang, H., and Chen, D.: The observation and characteristic analysis of sea-land breeze circulation in Xiamen area, *Straits Science*,
764 12, 3-7, 2017.
- 765 Yabushita, A., Enami, S., Sakamoto, Y., Kawasaki, M., Hoffmann, M. R., and Colussi, A. J.: Anion-Catalyzed Dissolution of NO₂ on
766 Aqueous Microdroplets, *J. Phys. Chem. A*, 113, 4844-4848, 2009.

767 Ye, C., Zhang, N., Gao, H., and Zhou, X.: Photolysis of Particulate Nitrate as a Source of HONO and NO_x, *Environ. Sci. Technol.*, 51, 6849-
768 6856, 10.1021/acs.est.7b00387, 2017.

769 Ye, C., Zhou, X., Pu, D., Stutz, J., Festa, J., Spolaor, M., Tsai, C., Cantrell, C., Mauldin, R. L., 3rd, Campos, T., Weinheimer, A., Hornbrook,
770 R. S., Apel, E. C., Guenther, A., Kaser, L., Yuan, B., Karl, T., Haggerty, J., Hall, S., Ullmann, K., Smith, J. N., Ortega, J., and Knote, C.:
771 Rapid cycling of reactive nitrogen in the marine boundary layer, *Nature*, 532, 489-491, 10.1038/nature17195, 2016.

772 Yu, Y., Galle, B., Panday, A., Hodson, E., Prinn, R., and Wang, S.: Observations of high rates of NO₂-HONO conversion in the nocturnal
773 atmospheric boundary layer in Kathmandu, Nepal, *Atmos. Chem. Phys.*, 9 6401-6415, 2009.

774 Zhang, B. and Tao, F.-M.: Direct homogeneous nucleation of NO₂, H₂O, and NH₃ for the production of ammonium nitrate particles and
775 HONO gas, *Chem. Phys. Lett.*, 489, 143-147, 10.1016/j.cplett.2010.02.059, 2010.

776 Zheng, J., Shi, X., Ma, Y., Ren, X., Jabbour, H., Diao, Y., Wang, W., Ge, Y., Zhang, Y., and Zhu, W.: Contribution of nitrous acid to the
777 atmospheric oxidation capacity in an industrial zone in the Yangtze River Delta region of China, *Atmos. Chem. Phys.*, 20, 5457-5475,
778 10.5194/acp-20-5457-2020, 2020.

779 Zhou, L., Wang, W., Hou, S., Tong, S., and Ge, M.: Heterogeneous uptake of nitrogen dioxide on Chinese mineral dust, *J. Environ. Sci.*
780 (China), 38, 110-118, 10.1016/j.jes.2015.05.017, 2015.

781 Zhou, X., Huang, G., Civerolo, K., Roychowdhury, U., and Demerjian, K. L.: Summertime observations of HONO, HCHO, and O₃ at the
782 summit of Whiteface Mountain, New York, *J. Geophys. Res.*, 112, 10.1029/2006jd007256, 2007.

783 Zhou, X., Zhang, N., TerAvest, M., Tang, D., Hou, J., Bertman, S., Alaghmand, M., Shepson, P. B., Carroll, M. A., Griffith, S., Dusanter,
784 S., and Stevens, P. S.: Nitric acid photolysis on forest canopy surface as a source for tropospheric nitrous acid, *Nat. Geosci.*, 4, 440-443,
785 10.1038/ngeo1164, 2011.

786

787 **Figure Captions**

788 **Figure 1.** Location of Xiamen in China (left) and surroundings of IUE.

789 **Figure 2.** Time series of relative humidity (RH), temperature (T), $J(\text{HONO})$, UV, HONO, NO_2 , NO, NO_3^- , $\text{PM}_{2.5}$, O_3 , and black carbon (BC)
790 in Xiamen, China in August, October, and December 2018, and March 2019. The missing data is mainly due to instrument maintenance.

791 **Figure 3.** Diurnal variations in (a) HONO, (b) NO (hollow markers and dashed lines) & NO_x (solid markers/lines), (c) HONO/ NO_x , and (d)
792 $J(\text{NO}_2)$. The gray shading indicates nighttime (18:00–06:00, including 18:00).

793 **Figure 4.** Scatter plots of NO_2 versus HONO color coded by $J(\text{NO}_2)$. The three dashed lines represent 10 %, 5 %, and 1 % ratios of
794 HONO/ NO_2 . Daytime was 06:00–18:00 LT, including 06:00.

795 **Figure 5.** Scatter plots of nighttime $\text{HONO}_{\text{corr}}/\text{NO}_2$ ratios versus RH. The average top-five $\text{HONO}_{\text{corr}}/\text{NO}_2$ in every 5 % RH interval are
796 shown as orange squares, and the error bars show ± 1 SD.

797 **Figure 6.** The correlation between the NH_3 concentration and HONO/ NO_2 ratio (upper) and the correlation between the NH_3 concentration
798 and the $\text{NO}_3^-/\text{NO}_2$ (lower) in four seasons. The scatter points were colored by ambient RH values.

799 **Figure 7.** The correlation between $\text{PM}_{2.5}$ and $\text{HONO}_{\text{corr}}$ (left) and the correlation between $\text{PM}_{2.5}$ and $\text{HONO}_{\text{corr}}/\text{NO}_2$ (right). The squares
800 depict $\text{PM}_{2.5} \geq 35 \mu\text{g}\cdot\text{m}^{-3}$; all scattered points are from the time when the ratio of $\text{HONO}_{\text{corr}}/\text{NO}_2$ reached a pseudo-steady state each night
801 (03:00–06:00 LT).

802 **Figure 8.** Average diurnal variations of each source (>0) and sink (<0) of HONO in the four seasons.

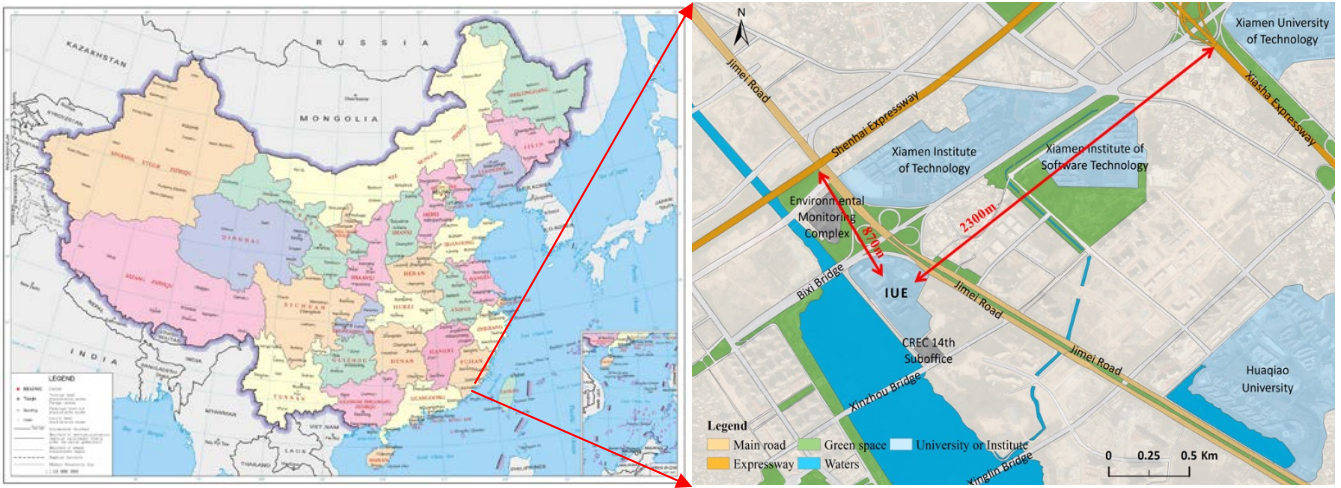
803 **Figure 9.** Relationships between the photolysis of particulate nitrate and R_{unknown} , colored by BC in spring, summer, autumn, and winter.
804 Red lines and dashed lines represent logarithmic fitting curve and turning point, respectively.

805 **Figure 10.** The ratio of HONO/ NO_x in the four seasons (correlation between the average of NO_x per 10 ppb interval and the average value
806 of HONO).

807 **Figure 11.** The diurnal variations in the measured values of HONO (black squares), the estimated values of HONO using the parameterized
808 formula (red circles), and the estimated values of HONO using the parameterized formula combined with the main daytime sources (green
809 triangles).

810 **Figure 12.** Comparison of OH formation by photolysis of HONO and O_3 in the four seasons.

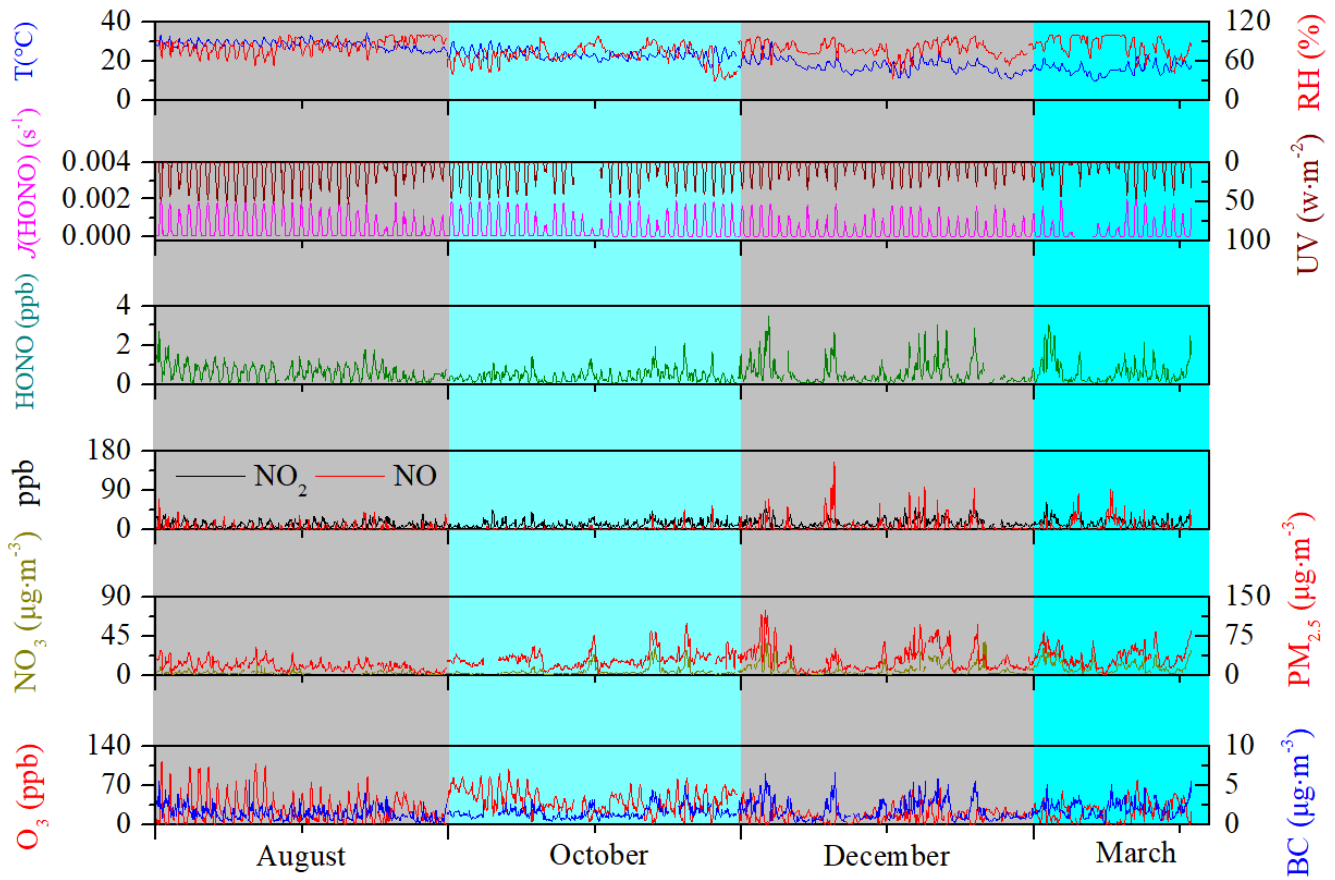
811



812 **Figure 1.** Location of Xiamen in China (left) and surroundings of IUE (right).

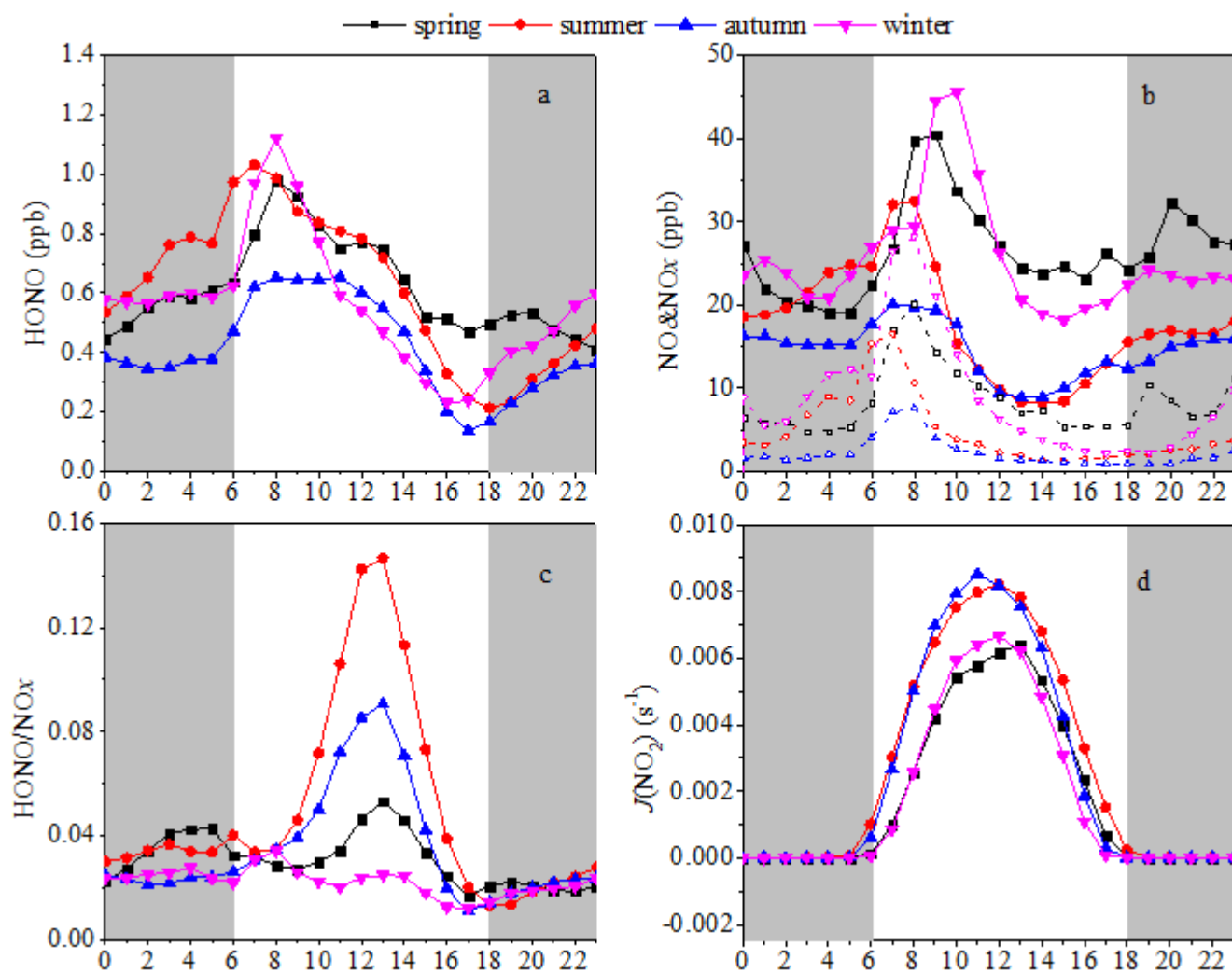
813 Note: The map in the left was directly download from <http://bzdt.ch.mnr.gov.cn/>, while the map in the right was significantly

814 enriched based on layer download from <http://www.rivermap.cn/>.



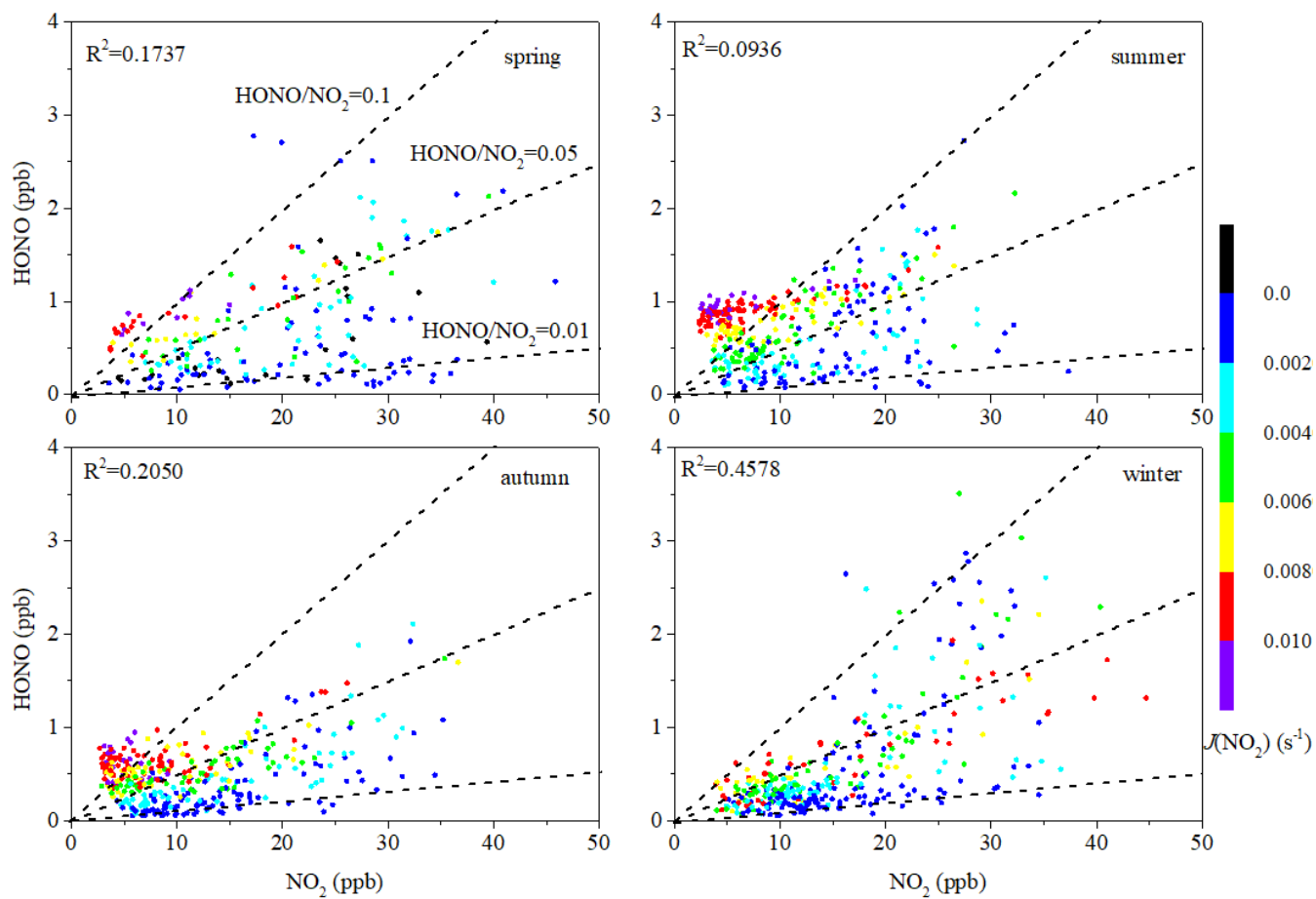
815

816 **Figure 2.** Time series of relative humidity (RH), temperature (T), $J(\text{HONO})$, UV, HONO, NO_2 , NO, NO_3^- , $\text{PM}_{2.5}$, O_3 , and black carbon (BC)
 817 in Xiamen, China in August, October, and December 2018, and March 2019. The missing data is mainly due to instrument maintenance.



819

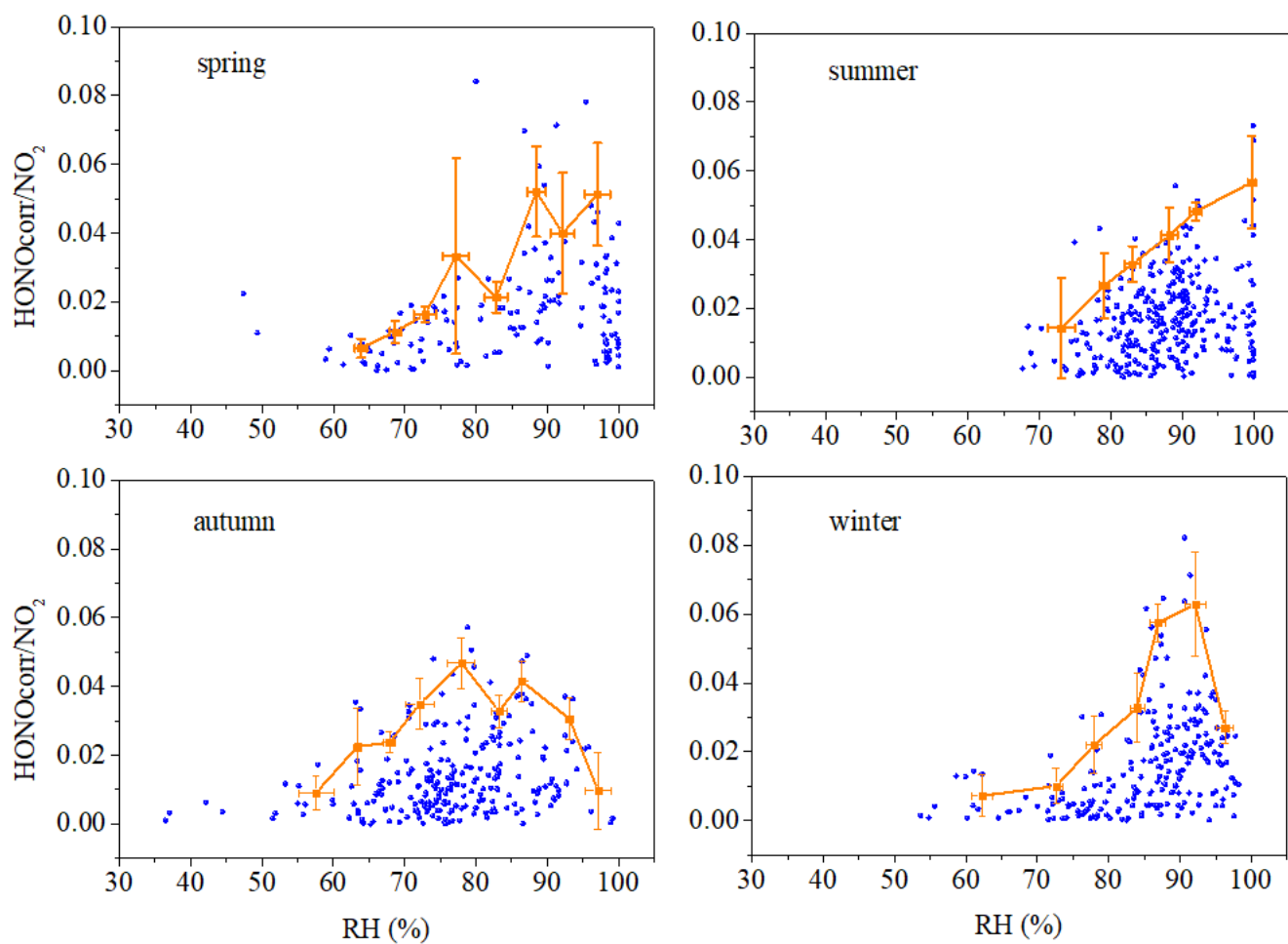
820 **Figure 3.** Diurnal variations in (a) HONO, (b) NO (hollow markers and dashed lines) & NOx (solid markers/lines), (c) HONO/NOx, and (d)
 821 $J(\text{NO}_2)$. The gray shading indicates nighttime (18:00–06:00, including 18:00).



822

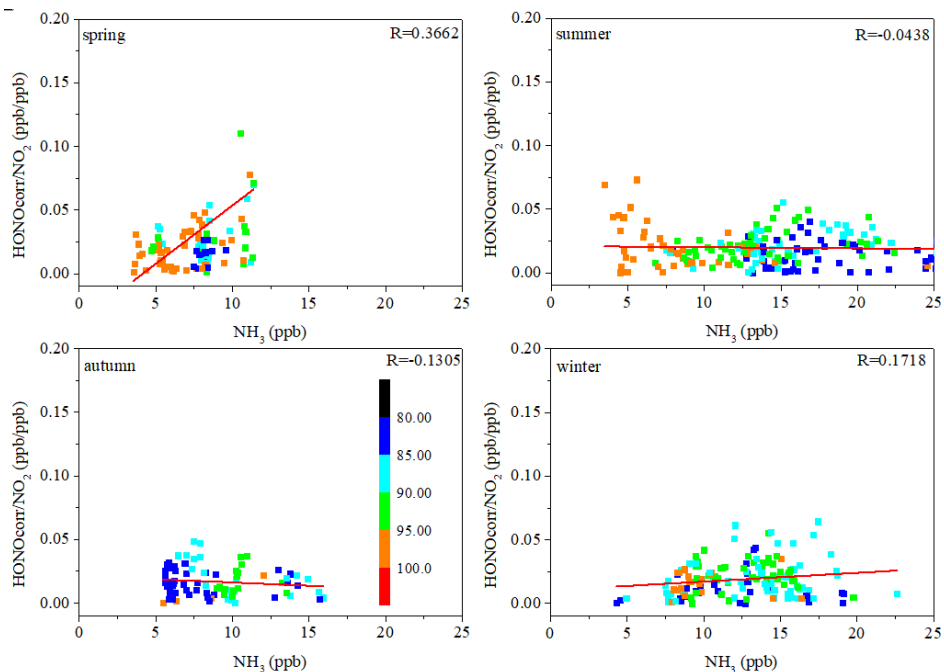
823 **Figure 4.** Scatter plots of NO₂ versus HONO color coded by $J(\text{NO}_2)$. The three dashed lines represent 10 %, 5 %, and 1 % ratios of
 824 HONO/NO₂. Daytime was 06:00–18:00 LT, including 06:00.

825

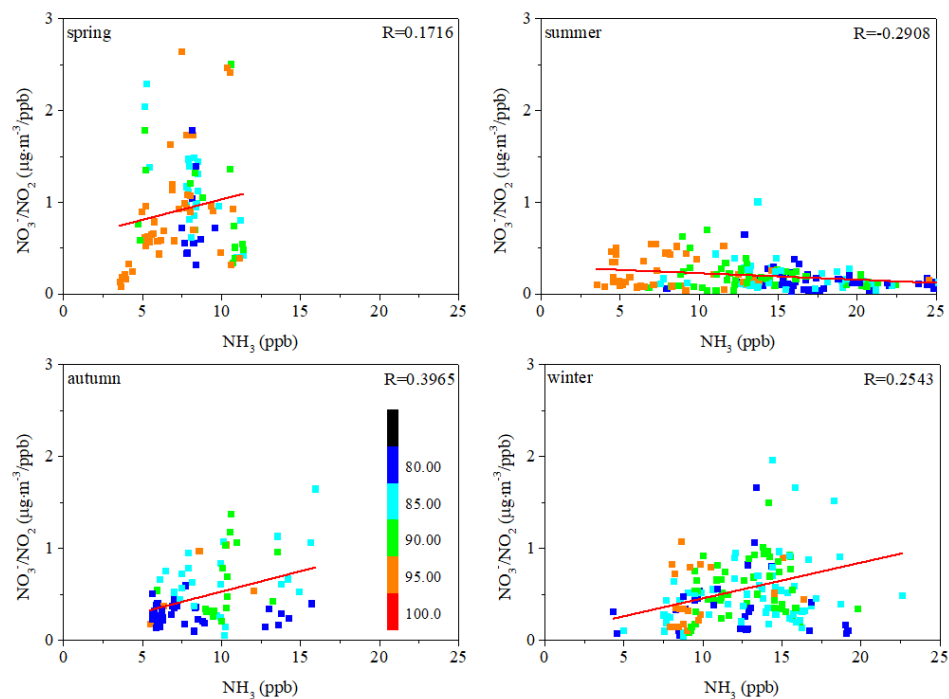


827

828 **Figure 5.** Scatter plots of nighttime $\text{HONO}_{\text{corr}}/\text{NO}_2$ ratios versus RH. The average top-five $\text{HONO}_{\text{corr}}/\text{NO}_2$ in every 5 % RH interval are
 829 shown as orange squares, and the error bars show ± 1 SD.

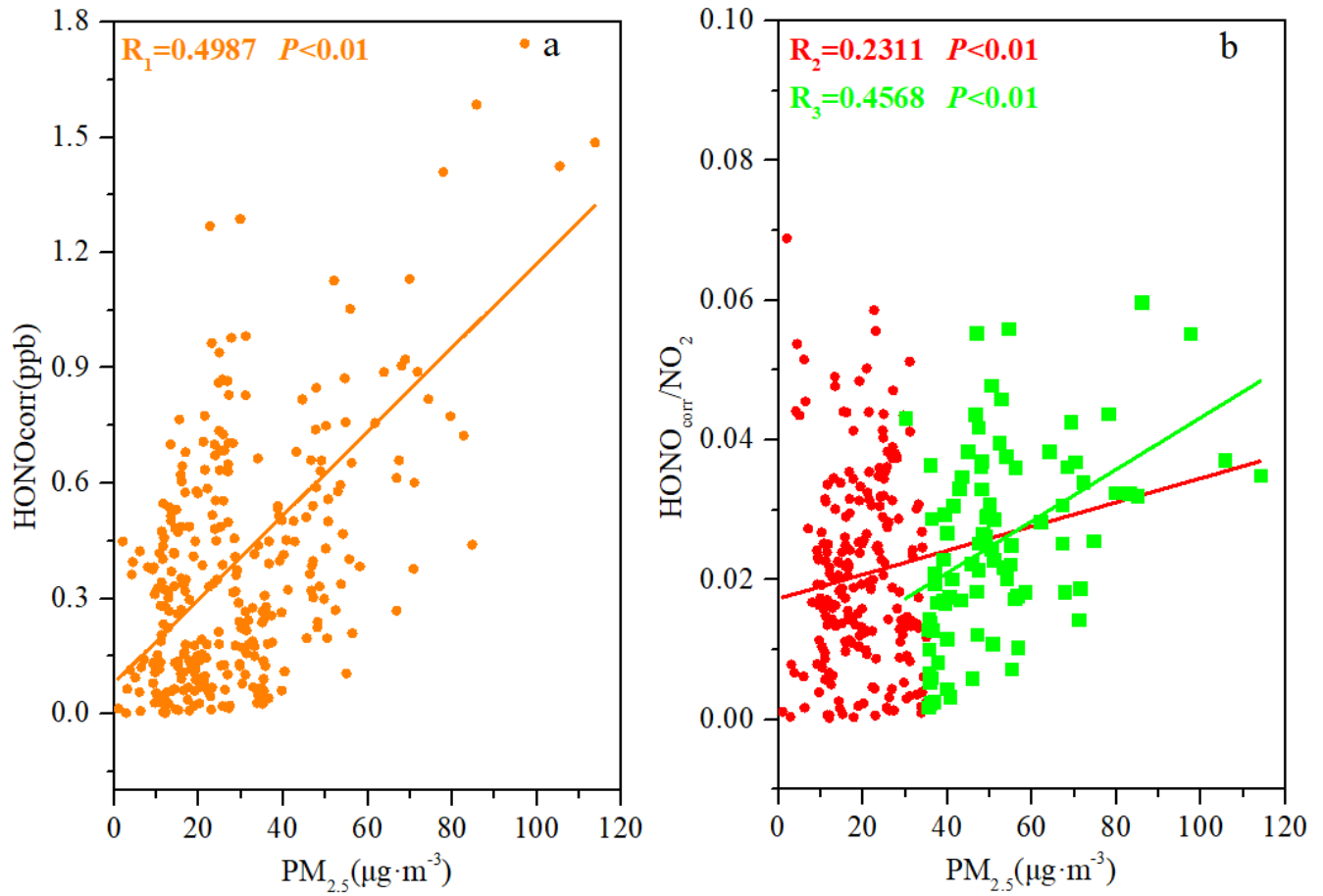


830



831

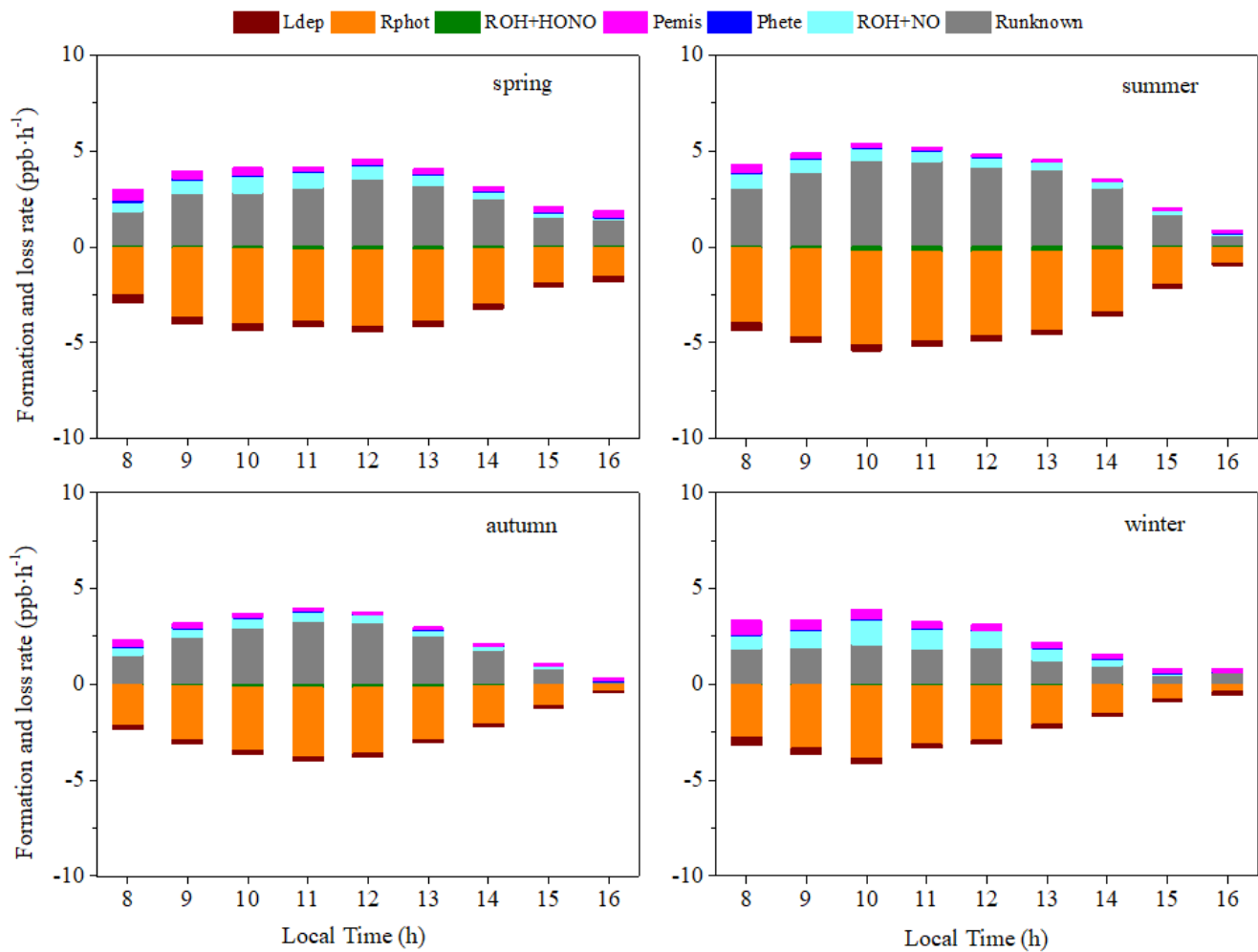
832 **Figure 6.** The correlation between the NH_3 concentration and HONO/NO_2 ratio (upper) and the correlation between the NH_3 concentration
 833 and the $\text{NO}_3^-/\text{NO}_2$ (lower) in four seasons. The scatter points were colored by ambient RH values.



835

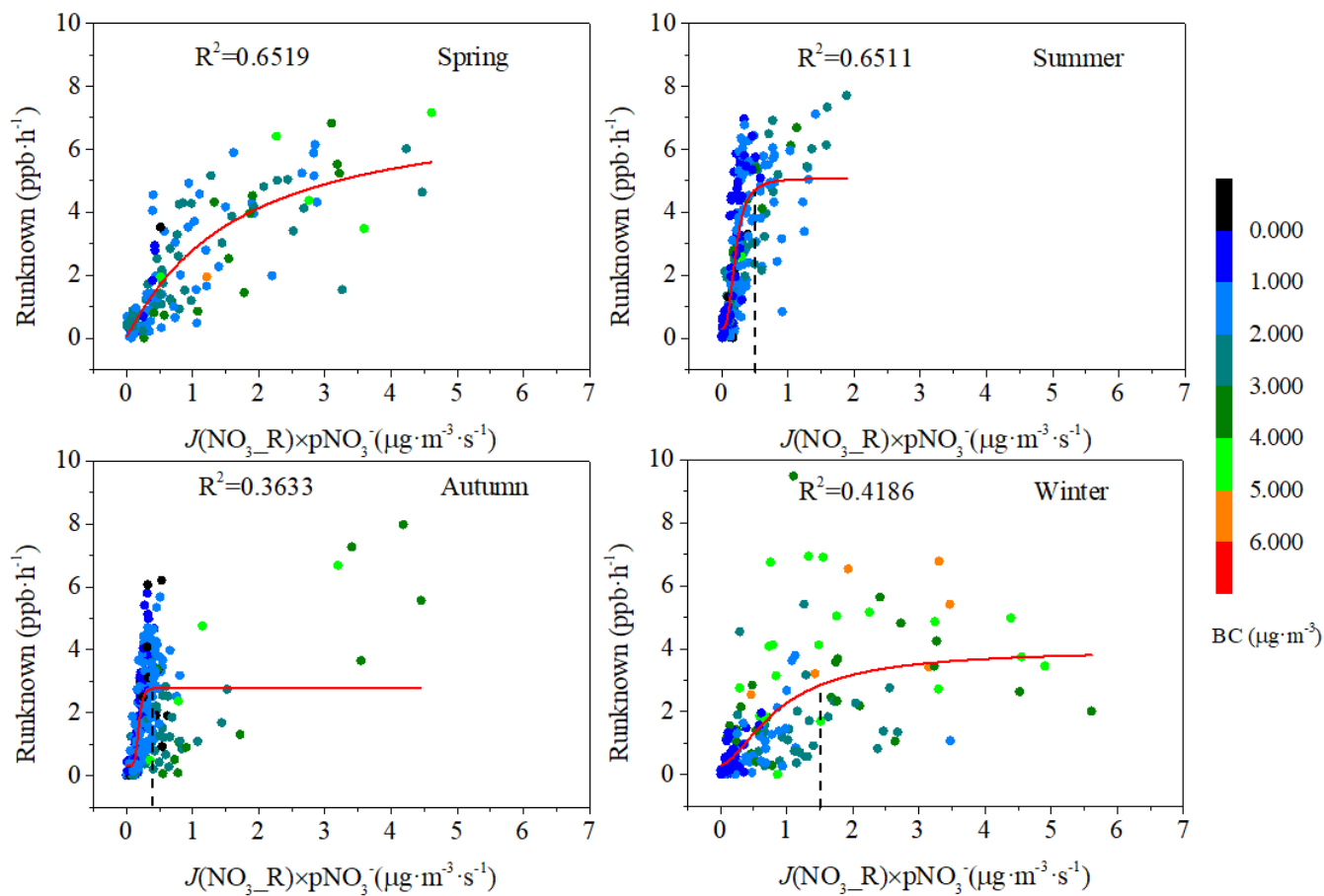
836 **Figure 7.** The correlation between $PM_{2.5}$ and $\text{HONO}_{\text{corr}}$ (left) and the correlation between $PM_{2.5}$ and $\text{HONO}_{\text{corr}}/\text{NO}_2$ (right). The squares
 837 depict $PM_{2.5} \geq 35 \mu\text{g}\cdot\text{m}^{-3}$; all scattered points are from the time when the ratio of $\text{HONO}_{\text{corr}}/\text{NO}_2$ reached a pseudo-steady state each night
 838 (03:00–06:00 LT).

839



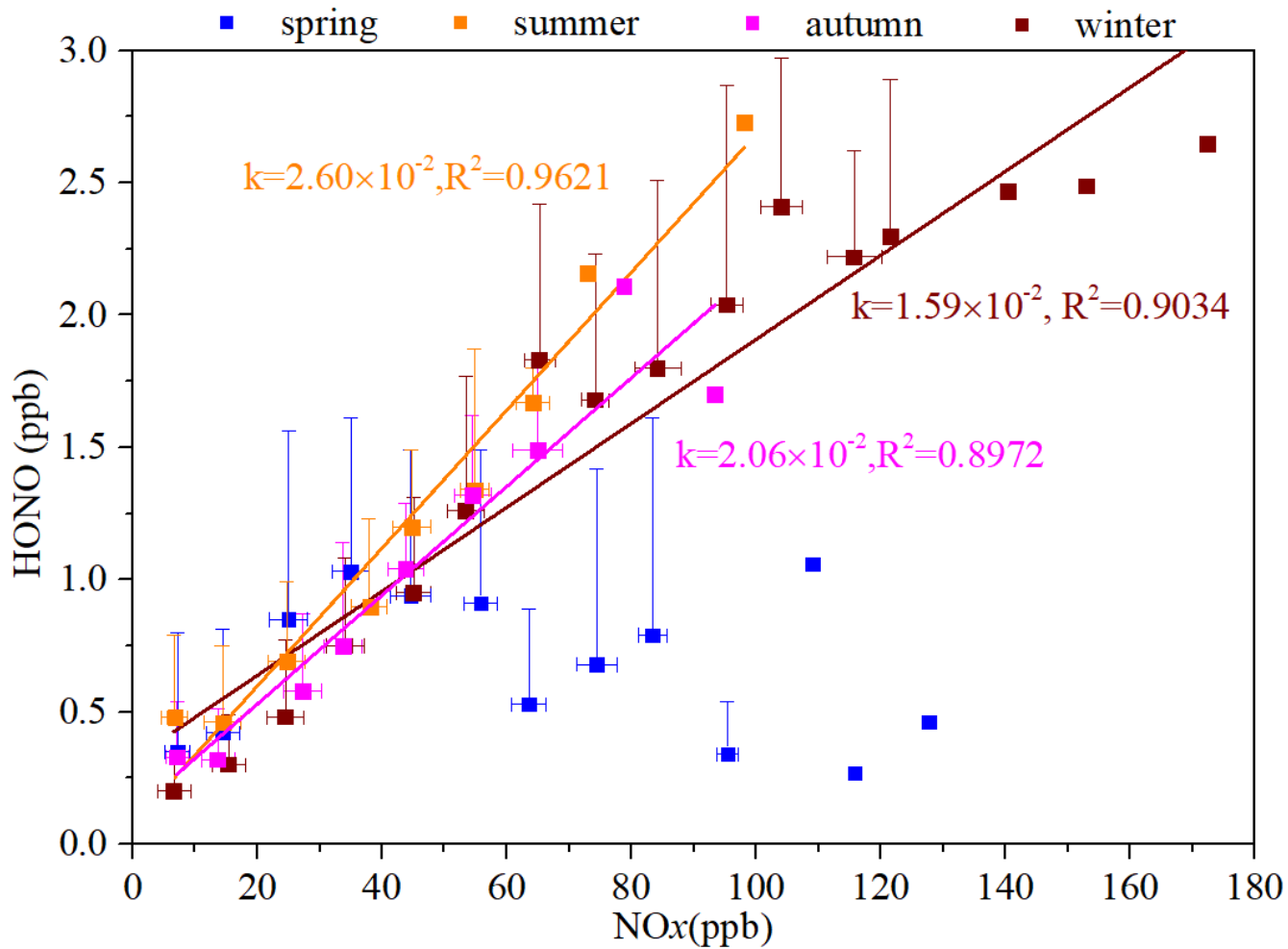
840

841 **Figure 8.** Average diurnal variations of each source (>0) and sink (<0) of HONO in the four seasons.



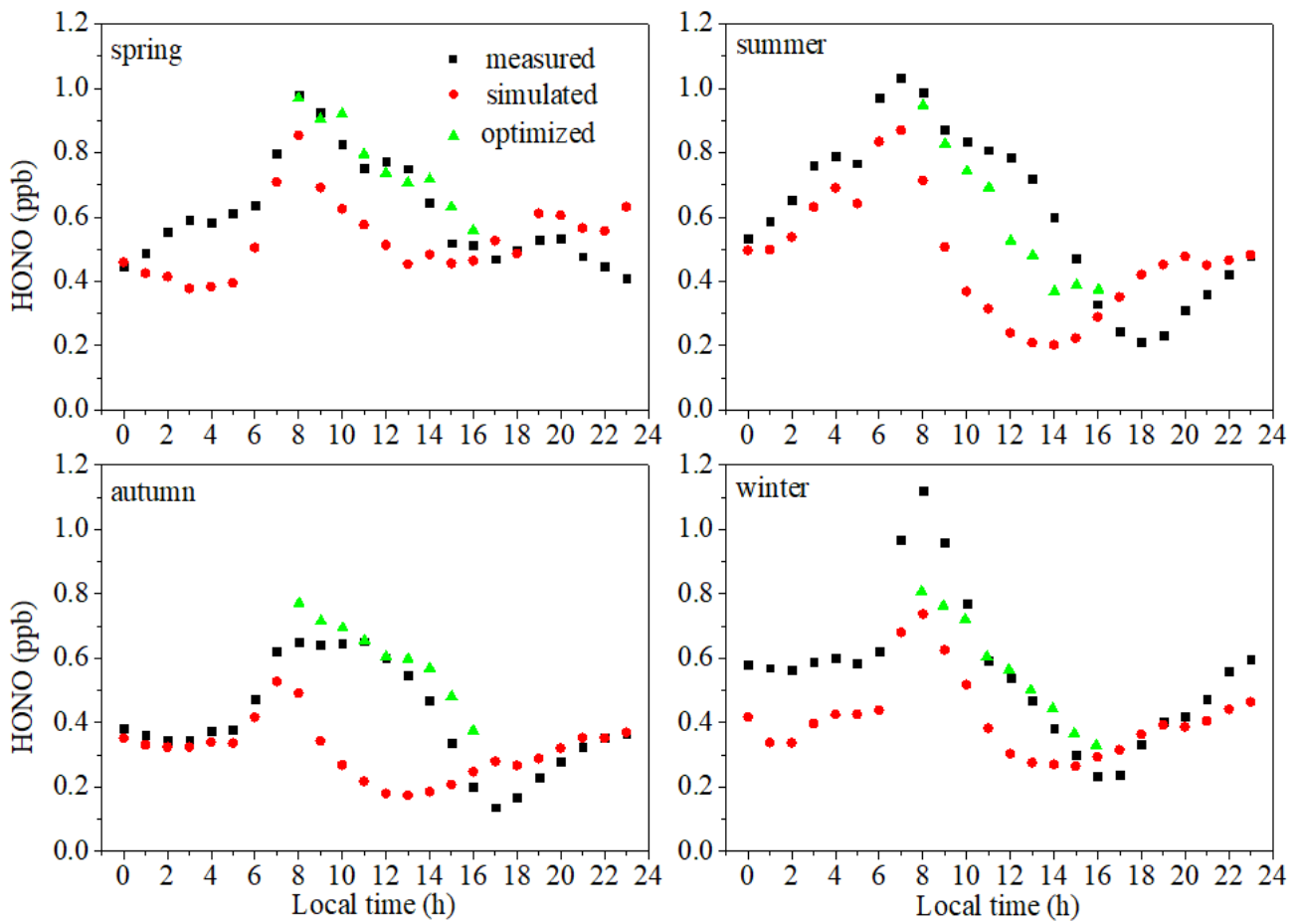
842

843 **Figure 9.** Relationships between the photolysis of particulate nitrate and R_{unknown} , colored by BC in spring, summer, autumn, and winter.
 844 Red lines and dashed lines represent logarithmic fitting curve and turning point, respectively.



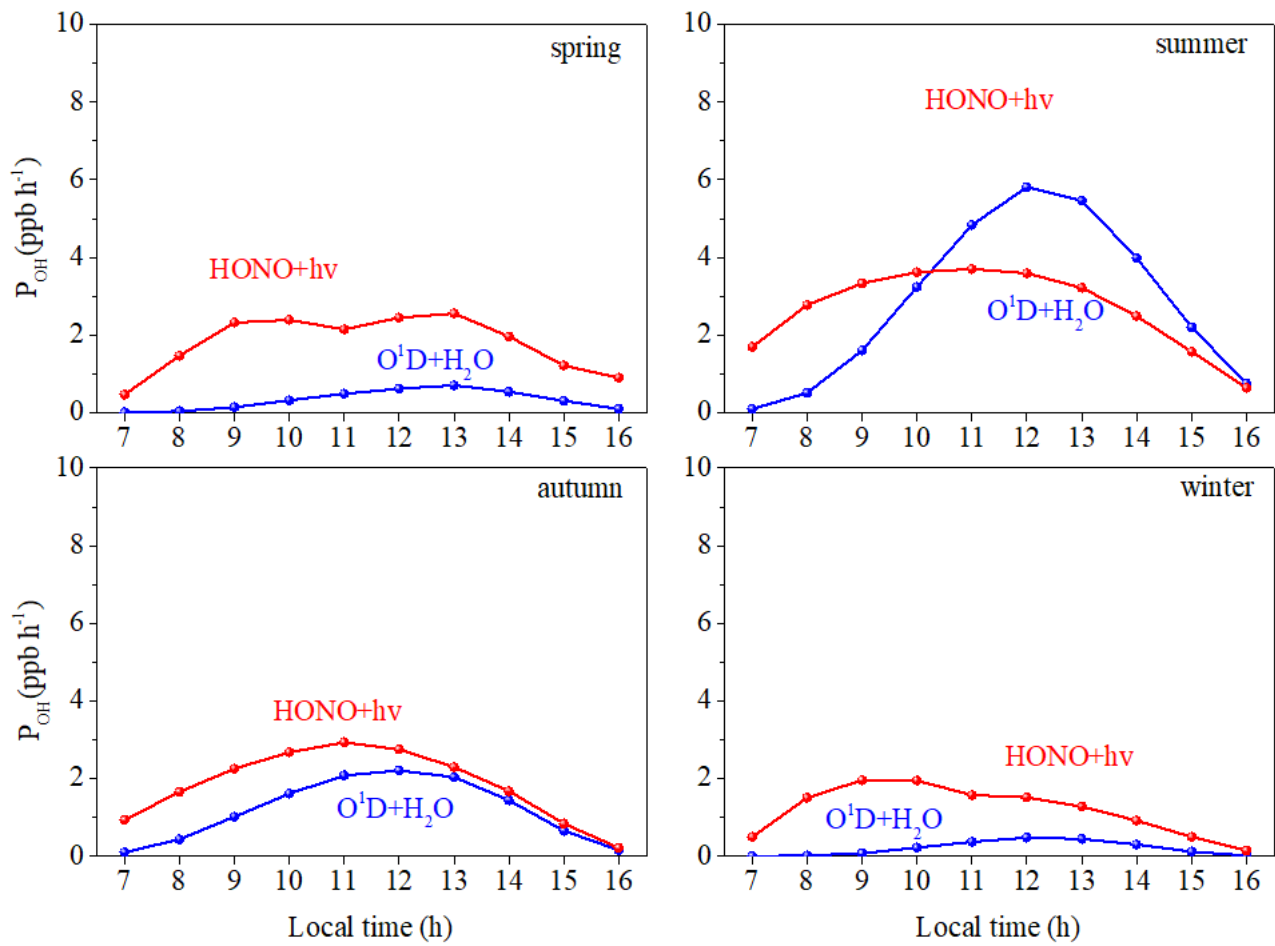
845

846 **Figure 10.** The ratio of HONO/NO_x in the four seasons (correlation between the average of NO_x per 10 ppb interval and the average value
 847 of HONO).



848

849 **Figure 11.** The diurnal variations in the measured values of HONO (black squares), the estimated values of HONO using the parameterized
 850 formula (red circles), and the estimated values of HONO using the parameterized formula combined with the main daytime sources (green
 851 triangles).



852

853 **Figure 12.** Comparison of OH formation by photolysis of HONO and O_3 in the four seasons.

854

855 **Tables**

856 **Table 1.** Overview of the HONO and NO_x average concentrations measured in Xiamen and comparison with other
857 measurements.

858 **Table 2.** Emission ratios of fresh vehicle plumes $\Delta\text{HONO}/\Delta\text{NO}_x$.

859 **Table 3.** Overview of the conversion frequencies from NO₂ to HONO in Xiamen and comparisons with other studies.

Table 1. Overview of the HONO and NO_x average concentrations measured in Xiamen and comparison with other measurements.

Location	Date	HONO (ppb)		NO ₂ (ppb)		NO _x (ppb)		HONO/NO ₂		HONO/NO _x		Reference
		Day	Night	Day	Night	Day	Night	Day	Night	Day	Night	
Xiamen/China (suburban)	Aug.2018- Mar.2019	0.63	0.46	13.6	16.3	20.9	19.9	0.061	0.028	0.046	0.024	This work
	Mar.2019(spring)	0.72	0.51	18.5	17.7	28.6	24.5	0.046	0.032	0.034	0.028	
	Aug.2018(summer)	0.72	0.51	11.0	15.7	16.6	18.9	0.094	0.031	0.072	0.027	
	Oct.2018(autumn)	0.50	0.33	11.4	14.3	14.1	15.1	0.060	0.023	0.048	0.022	
	Dec.2018(winter)	0.61	0.52	15.8	18.3	28.0	23.1	0.036	0.026	0.023	0.022	
Jinan/China (urban)	Sep 2015-Aug 2016	0.99	1.28	25.8	31.0	40.6	46.4	0.056	0.079	0.035	0.040	(Li et al., 2018a)
	Sep.-Nov. 2015 (autumn)	0.66	0.87	23.2	25.4	37.5	38.0	0.034	0.049	0.022	0.034	
	Dec.2015- Feb.2016(winter)	1.35	2.15	34.6	41.1	64.8	78.5	0.047	0.056	0.031	0.034	
	Mar.-May 2016 (spring)	1.04	1.24	25.8	35.8	36.0	47.3	0.052	0.046	0.041	0.035	
	Jun.-Aug. 2016 (summer)	1.01	1.20	19.0	22.5	25.8	29.1	0.079	0.106	0.049	0.060	
Nanjing/China (suburban)	Nov. 2017-Nov. 2018	0.57	0.80	13.9	18.9	19.3	24.9	0.044	0.045	0.036	0.041	(Liu et al., 2019a)
	Dec.-Feb. (winter)	0.92	1.15	23.1	28.4	37.7	45.5	0.038	0.040	0.025	0.029	
	Mar.-May (spring)	0.59	0.76	12.9	17.4	15.9	19.1	0.049	0.048	0.042	0.046	
	Jun.-Aug. (summer)	0.34	0.56	7.7	12.5	9.1	13.5	0.051	0.048	0.045	0.046	
Hongkong/China	Sep.-Nov. (autumn)	0.51	0.81	13.4	18.9	17.7	25.1	0.035	0.044	0.029	0.039	(Xu et al., 2015)
	Aug.2011(summer)	0.70	0.66	18.1	21.8	29.3	29.3	0.042	0.031	0.028	0.025	
	Nov.2011(autumn)	0.89	0.95	29.0	27.2	40.6	37.2	0.030	0.034	0.021	0.028	
	Feb.2012(winter)	0.92	0.88	25.8	22.2	48.3	37.8	0.035	0.036	0.020	0.025	
Guangzhou/China (urban)	May2012(spring)	0.40	0.33	15.0	14.7	21.1	19.1	0.030	0.022	0.022	0.019	(Qin et al., 2009)
Jun.2006	2.00	3.50	30.0	20.0	-	-	0.067	0.175	-	-		
Xi'an/China	Jul.-Aug.2015	1.57	0.51	24.7	15.4	-	-	0.062	0.033	-	-	(Huang et al., 2017)
Santiago/Chile (urban)	Mar.-Jun.2005	1.50	3.00	20.0	30.0	40.0	200.0	0.075	0.100	0.038	0.015	(Elshorbany et al., 2009)
Rome/Italy (urban)	May-Jun.2001	0.15	1.00	4.0	27.2	4.2	51.2	0.038	0.037	0.024	0.020	(Acker et al., 2006)
Kathmandu/Nepal (urban)	Jan.-Feb.2003	0.35	1.74	8.6	17.9	13.0	20.1	0.041	0.097	0.027	0.087	(Yu et al., 2009)

862 Note: Night (18:00-6:00, including 18:00, local time); Day (6:00-18:00, including 6:00, local time)

863 NO_x=NO₂ (IBBCEAS)+NO (Thermal 42i). IBBCEAS measure both HONO and NO₂. The NO₂ concentration is always overestimated by
864 the Thermo Fisher 42i.

Date	Time	$\Delta\text{NO}/\Delta\text{NO}_x$	R^2	$\Delta\text{HONO}/\Delta\text{NO}_x$ (%)
2018/8/1	7:00-8:55	1.1621	0.6897	2.17
2018/8/8	5:40-5:55	0.8727	0.8023	2.69
2018/8/21	5:00-5:55	0.8571	0.7553	1.14
2018/8/31	23:35-23:55	1.1861	0.8130	1.18
2018/10/23	1:05-1:25	0.9893	0.6566	1.27
2018/12/4	7:20-7:40	0.9594	0.8502	1.11
2018/12/10	11:00-11:15	0.8778	0.6735	1.79
2018/12/11	0:00-0:50	0.9424	0.6972	0.58
2018/12/11	4:00-4:55	0.9652	0.7686	2.12
2018/12/11	5:45-6:35	1.0243	0.6566	0.84
2018/12/11	6:40-7:40	0.9992	0.7067	1.59
2018/12/20	22:50-23:10	0.9811	0.7736	0.97
2018/12/21	0:45-1:15	1.0029	0.8914	1.54
2018/12/22	6:40-7:35	1.0194	0.7010	2.36
2018/12/22	7:40-8:05	0.9932	0.7831	2.94
2018/12/25	21:00-22:10	0.9573	0.8857	1.64
2018/12/26	3:50-4:15	1.167	0.6540	1.39
2018/12/26	6:45-7:45	0.9971	0.8463	0.92
2018/12/26	7:55-8:25	0.9714	0.6919	2.95
2018/12/27	4:50-5:30	0.9365	0.7265	0.76
2019/3/6	7:30-8:05	1.0309	0.8283	0.74
2019/3/9	7:50-8:05	0.9933	0.9203	0.24
2019/3/9	12:00-12:55	0.9627	0.6444	0.51

867 **Table 3.** Overview of the conversion frequencies from NO₂ to HONO in Xiamen and comparisons with other studies.

Location	Date	Conversion rate (% h-1)	Reference
Xiamen/China	Aug.2018-Mar.2019	0.46	This study
	Mar.2019(spring)	0.46	
	Aug.2018(summer)	0.55	
	Oct.2018(autumn)	0.44	
	Dec.2018(winter)	0.37	
Xinken/China	Oct.-Nov.,2004	1.60	(Su et al., 2008b)
Jinan/China	Sep.,2015-Aug.,2016	0.68	(Li et al., 2018a)
	Mar.-May 2016(spring)	0.43	
	Jun.-Aug. 2016(summer)	0.69	
	Sep.-Nov. 2015(autumn)	0.75	
	Dec.2015-Feb. 2016(winter)	0.83	
Guangzhou/China	Jun.,2006	2.40	(Li et al., 2012)
Spain	Nov.-Dec.,2008	1.50	(Sörgel et al., 2011)
Beijing/China	Sep.2015-July 2016	0.80	(Wang et al., 2017)
	Apr.-May, 2016 (spring)	0.50	
	Jun.-Jul., 2016 (summer)	1.00	
	Sep.-Oct. 2015 (autumn)	0.90	
	Jan.2016 (winter)	0.60	
Shandong/China	Nov.2013-Jan.2014	0.29	(Wang et al., 2015)
Shanghai/China	Aug.2010-Jun.2012	0.70	(Wang et al., 2013)
Eastern Bohai Sea/China	Oct.-Nov., 2016	1.80	(Wen et al., 2019)
Hongkong/China	Aug.2011-May, 2012	0.52	(Xu et al., 2015)
Kathmandu/South Asia	Jan.-Feb.,2003	1.4	(Yu et al., 2009)